

PACS photometry of the *Herschel* Reference Survey – Far-infrared/sub-millimeter colours as tracers of dust properties in nearby galaxies*

L. Cortese^{†1,2}, J. Fritz³, S. Bianchi⁴, A. Boselli⁵, L. Ciesla⁶, G. J. Bendo⁷, M. Boquien^{5,8}, H. Roussel⁹, M. Baes³, V. Buat⁵, M. Clemens¹⁰, A. Cooray¹¹, D. Cormier¹², J. I. Davies¹³, I. De Looze³, S. A. Eales¹³, C. Fuller¹³, L. K. Hunt⁴, S. Madden¹⁴, J. Munoz-Mateos¹⁵, C. Pappalardo⁴, D. Pierini¹⁶, A. Rémy-Ruyer¹⁴, M. Sauvage¹⁴, S. di Serego Alighieri⁴, M. W. L. Smith¹³, L. Spinoglio¹⁷, M. Vaccari¹⁸, C. Vlahakis¹⁹

¹Centre for Astrophysics & Supercomputing, Swinburne University of Technology, Mail H30 - PO Box 218, Hawthorn, VIC 3122, Australia

²European Southern Observatory, Karl-Schwarzschild Str. 2, 85748 Garching bei Muenchen, Germany

³Sterrenkundig Observatorium, Universiteit Gent, Krijgslaan 281 S9, 9000, Gent, Belgium

⁴INAF-Osservatorio Astrofisico di Arcetri, Largo Enrico Fermi 5, 50125 Firenze, Italy

⁵Laboratoire d'Astrophysique de Marseille - LAM, Université d'Aix-Marseille & CNRS, UMR7326, 38 rue F. Joliot-Curie, F-13388 Marseille Cedex 13, France

⁶University of Crete, Department of Physics, Heraklion, Crete, 71003, Greece

⁷UK ALMA Regional Centre Node, Jodrell Bank Centre for Astrophysics, School of Physics and Astronomy, University of Manchester, Oxford Road, Manchester M13 9PL, United Kingdom

⁸Institute of Astronomy, University of Cambridge, Madingley Road, Cambridge CB30HA, UK

⁹Institut d'Astrophysique de Paris, Université Pierre et Marie Curie (UPMC), CNRS (UMR7095), 75014 Paris, France

¹⁰Osservatorio Astronomico di Padova, Vicolo dell'Osservatorio 5, I-35122 Padova, Italy

¹¹University of California, Irvine, Department of Physics & Astronomy, 4186 Frederick Reines Hall, Irvine, CA, USA

¹²Institut für Theoretische Astrophysik, Zentrum für Astronomie der Universität Heidelberg, Albert-Ueberle Str. 2, D-69120 Heidelberg, Germany

¹³School of Physics and Astronomy, Cardiff University, The Parade, Cardiff, CF24 3AA, UK

¹⁴Laboratoire AIM, CEA, Université Paris VII, IRFU/Service d'Astrophysique, Bat. 709, 91191 Gif-sur-Yvette, France

¹⁵European Southern Observatory, Alonso de Cordova 3107, Vitacura, Casilla 19001, Santiago de Chile

¹⁶Max-Planck-Institut für extraterrestrische Physik, Giessenbachstrasse, Postfach 1312, D-85741, Garching bei München, Germany

¹⁷Istituto di Fisica dello Spazio Interplanetario, INAF, Via Fosso del Cavaliere 100, I-00133 Roma, Italy

¹⁸Astrophysics Group, Physics Department, University of the Western Cape, Private Bag X17, Bellville 7535, Cape Town, South Africa

¹⁹Joint ALMA Observatory/European Southern Observatory, Alonso de Cordova 3107, Vitacura, Santiago, Chile

Accepted 2014 January 21. Received 2014 January 20; in original form 2013 November 3

ABSTRACT

We present *Herschel*/PACS 100 and 160 μm integrated photometry for the 323 galaxies in the *Herschel* Reference Survey (HRS), a K-band-, volume-limited sample of galaxies in the local Universe. Once combined with the *Herschel*/SPIRE observations already available, these data make the HRS the largest representative sample of nearby galaxies with homogeneous coverage across the 100–500 μm wavelength range. In this paper, we take advantage of this unique dataset to investigate the properties and shape of the far-infrared/sub-millimeter spectral energy distribution in nearby galaxies. We show that, in the stellar mass range covered by the HRS ($8 \leq \log(M_*/M_\odot) \leq 12$), the far-infrared/sub-millimeter colours are inconsistent with a single modified black-body having the same dust emissivity index β for all galaxies. In particular, either β decreases, or multiple temperature components are needed, when moving from metal-rich/gas-poor to metal-poor/gas-rich galaxies. We thus investigate how the dust temperature and mass obtained from a single modified black-body depend on the assumptions made on β . We show that, while the correlations between dust temperature, galaxy structure and star formation rate are strongly model dependent, the dust mass scaling relations are much more reliable, and variations of β only change the strength of the observed trends.

Key words: galaxies: fundamental parameters – galaxies: ISM – infrared: galaxies

1 INTRODUCTION

It is now well established that approximately half of the radiative energy produced by galaxies is absorbed by dust grains and re-emitted in the infrared regime (Hauser & Dwek 2001; Boselli et al. 2003; Dole et al. 2006; Dale et al. 2007; Burgarella et al. 2013). Thus, observations in the $\sim 10\text{--}1000\ \mu\text{m}$ wavelength range provide us with a unique opportunity not only to quantify half of the bolometric luminosity of galaxies, but also to characterise the properties of cosmic dust. Moreover, since dust grains are crucial for the star formation cycle (Hollenbach & Salpeter 1971), such information can give us important insights into the physical processes regulating galaxy evolution (e.g., Dunne et al. 2011).

Unfortunately, despite its paramount importance, we are still missing a complete and coherent picture of dust properties in galaxies across the Hubble sequence, and of the exact role played by grains in regulating star formation (McKee & Krumholz 2010). Indeed, we know very little about the dust composition in galaxies outside our own Local Group (Draine & Li 2007; Compiègne et al. 2011) and if/how it is regulated by the physical conditions experienced by grains in the inter-stellar medium (ISM). Hence, our estimates of dust masses in galaxies are still highly uncertain (Finkbeiner et al. 1999; Dupac et al. 2003; Gordon et al. 2010; Paradis et al. 2010; Planck Collaboration et al. 2011b).

Luckily, the last decade has seen the start of a golden age for observational far-infrared (FIR) and sub-millimeter (submm) astronomy, providing a new boost to the refinement of theoretical dust models (Meny et al. 2007; Draine & Li 2007; Hoang et al. 2010; Compiègne et al. 2011; Steinacker et al. 2013). In particular, the *Spitzer* (Werner et al. 2004), and more recently *Herschel* (Pilbratt et al. 2010) and *Planck* (Planck Collaboration et al. 2011a) space telescopes are finally gathering a wealth of information on the dust emission from thousands of galaxies up to $z \sim 2$. Particularly important for a proper characterisation of dust in galaxies is the radiation emitted at wavelengths $\gtrsim 100\text{--}200\ \mu\text{m}$. In this regime, the integrated emission from galaxies originates predominantly from dust in thermal equilibrium, heated by the diffuse interstellar radiation field (ISRF), which represents the bulk of the dust mass in a galaxy (e.g., Sodroski et al. 1989; Sauvage & Thuan 1992; Calzetti et al. 1995; Walterbos & Greenawalt 1996; Bendo et al. 2010; Boquien et al. 2011; Bendo et al. 2012). Thus, by characterising the dust emission in the $\gtrsim 100\ \mu\text{m}$ wavelength domain, we have a unique opportunity to provide strong constraints to theoretical models, and to refine our census of the dust budget in galaxies.

The first natural step in this direction is to quantify how the shape of the dust spectral energy distribution (SED) varies with galaxy properties across a wide range of morphological type, star formation activity, cold gas mass and metal content. This is necessary to determine if the amount of radiation emitted at each wavelength is simply regulated by the intensity of the ISRF responsible for the dust heating, or whether it retains an imprint of the chemical composition of the grains. Indeed, only after a careful characterisation of the physical parameters regulating the dust SED, will it be possible to properly convert observables into physical quantities such as dust temperatures and dust masses.

Many recent works (Gordon et al. 2010; Skibba et al. 2011; Davies et al. 2012; Planck Collaboration et al. 2011b; Galametz et al. 2012; Auld et al. 2013) have shown that, above $\sim 100\ \mu\text{m}$, the dust SED is very well approximated by a simple modified black-body (but see also Bendo et al. 2012):

$$F_\nu = \frac{M_{dust}}{D^2} \kappa_{\nu_0} \left(\frac{\nu}{\nu_0} \right)^\beta B_\nu(T) \quad (1)$$

where F_ν is the flux density emitted at the frequency ν , κ_{ν_0} is the dust mass absorption coefficient at the frequency ν_0 , β gives its variation as a function of frequency, D is the galaxy distance and $B_\nu(T)$ is the Planck function. Mounting evidence is emerging that β is not the same in all galaxies (e.g., Rémy-Ruyer et al. 2013), and may also vary within galaxies (e.g., Galametz et al. 2012; Smith et al. 2012).

Modified black-bodies are simple models and cannot properly reproduce real dust properties (e.g., Draine & Li 2007; Shetty et al. 2009; Bernard et al. 2010). Several dust components at various temperatures contribute to the total emission along the lines-of-sight. This implies the presence of temperature mixing that can cause variations of the infrared slope, and thus in the apparent emissivity index β . Nevertheless, parameterization of the dust SEDs through modified black-body fitting is a powerful tool to help understand variations of dust properties with other galaxy characteristics, especially in case of sparse sampling of the FIR/sub-mm wavelength range (e.g., high-redshift galaxies Magdis et al. 2011; Symeonidis et al. 2013). Therefore, it is extremely important to determine in which cases a single modified black-body can be used, and how temperature and dust mass estimates are affected by the assumptions made on β .

In order to ascertain the dust properties of galaxies in the local Universe, and to provide new constraints to theoretical models, we have carried out the *Herschel* Reference Survey (HRS, Boselli et al. 2010b), a *Herschel* guaranteed time project focused on the study of the interplay between dust, gas and star formation in a statistically significant sample of ~ 300 galaxies spanning a wide range of morphologies, stellar masses ($8 \lesssim \log(M_*/M_\odot) \lesssim 12$), cold gas contents ($-3 \lesssim \log(M_{HI}/M_*) \lesssim 1$), metallicities ($8.2 \lesssim 12 + \log(O/H) \lesssim 8.9$), and specific star formation rates ($-12 \lesssim \log(\text{SFR}/M_*) \lesssim -9$). The combination of *Herschel*/SPIRE (Griffin et al. 2010) observations with the multi-wavelength dataset we have been assembling (Ciesla et al. 2012; Cortese et al. 2012a;

* *Herschel* is an ESA space observatory with science instruments provided by European-led Principal Investigator consortia and with important participation from NASA.

† lcortese@swin.edu.au

Boselli et al. 2013; Hughes et al. 2013), has already allowed us to have a first glimpse at how the dust content and shape of the dust SED vary with internal galaxy properties (Boselli et al. 2010a, 2012; Cortese et al. 2012b). In particular, Boselli et al. (2010a, 2012) have shown that the slope of the dust SED in the 200-500 μm interval decreases from $\beta \sim 2$ to $\beta \sim 1$ when moving from metal-rich to metal-poor galaxies. However, our analyses have so far been limited by the lack of data in the ~ 100 -200 μm wavelength range for the entire sample.

Thus, in this paper we present integrated *Herschel*/PACS (Poglitsch et al. 2010) 100 and 160 μm flux densities for all the HRS sample and take advantage of our multiwavelength dataset to perform a first analysis of the properties of the dust SED across our entire sample. Corresponding to the peak of the dust SED, the 100-200 μm wavelength interval is crucial not only to properly quantify the shape of the SED, but also to accurately determine the average dust temperature and total dust mass in galaxies. These data make the HRS the largest representative sample of nearby galaxies with homogeneous coverage across the ~ 100 -500 μm wavelength range. In addition to releasing our dataset to the community, our primary goals are 1) to investigate how the shape of the dust SED varies with internal galaxy properties, and 2) to determine whether the integrated dust SED of HRS galaxies can always be reduced to a single modified black-body with a constant value of β and, if not, what are the possible biases introduced by this assumption. The results of SED fitting with the dust models of Draine et al. (2007) will be presented in a forthcoming paper (Ciesla et al., submitted.).

This paper is organized as follows. In Sect. 2 we describe the *Herschel* observations, data reduction, flux density estimates and comparison with the literature. In Sect. 3 we use the PACS and SPIRE colours to investigate how the shape of the dust SED varies with internal galaxy properties. In Sect. 4, we show how the dust temperature and mass obtained from fitting a single modified black-body to the *Herschel* data depend on the assumptions made on β . Finally, the summary and implications of our results are presented in Sec. 5.

2 THE DATA

2.1 The *Herschel* Reference Survey

The HRS is a volume-limited sample (i.e., $15 \leq D < 25$ Mpc) including all late-type galaxies (261 Sa and later) with 2MASS (Skrutskie et al. 2006) K-band magnitude $K_{S,tot} \leq 12$ mag and all early-type galaxies (62 S0a and earlier) with $K_{S,tot} \leq 8.7$ mag¹. Additional selection criteria are high galactic latitude ($b > +55^\circ$) and low Galactic extinction ($A_B < 0.2$ mag, Schlegel et al. 1998), to minimize Galactic cirrus contamination. More details on the original selection can be found in Boselli et al. (2010b), while the most recent morphological classifications and distance estimates are presented in Cortese et al. (2012a).

¹ We note that one galaxy (HRS228) had a wrong redshift reported in NED, and is in reality a background galaxy. In this work, we have included it for completeness.

2.2 PACS observations and data reduction

The *Herschel*/PACS 100 and 160 μm observations of HRS galaxies presented in this work have been obtained as part of various open-time *Herschel* projects.

The vast majority of the data (228 out of 323 galaxies) comes from our own *Herschel* cycle 1 open time proposal (OT1_l cortese1). Each galaxy was observed in scan mode, along two perpendicular axes, at the medium scan speed of 20''/sec. Two repetitions were done in each scan direction. The size of each map was chosen to match the size of our SPIRE images (see Ciesla et al. 2012), making sure to have homogeneous coverage across the entire 100-500 μm range.

Maps for additional 83 HRS galaxies have been obtained as part of the *Herschel* Virgo Cluster Survey (HeViCS, Davies et al. 2010). HeViCS mapped the Virgo cluster with both PACS and SPIRE simultaneously at the fast scan speed of 60''/sec. The observing strategy consists of scanning each $\sim 4 \times 4$ deg² field in two orthogonal directions, and repeating each scan four times (Auld et al. 2013). The faster scan speed of the *Herschel* parallel mode with respect to the scan map mode, used for our observations, is compensated by the higher number of repetitions performed in the Virgo cluster, making the two datasets highly comparable (i.e., within $\sim 30\%$) in terms of their final noise.

PACS observations for the remaining 12 HRS galaxies have been retrieved from the *Herschel* public archive, and come from various projects (i.e., Kennicutt et al. 2011, KPGT_esturm_1, OT1_acrocker_1, OT2_emurph01_3, GT1_lspinogl_2, OT2_aalonsoh_2). All data have been obtained in scan mode at the medium scan speed of 20''/sec and they reach a noise level similar or lower than our own observations. For one galaxy (HRS3) only 160 μm observations are available as the object lies at the edge of the 100 μm map, making the data not suitable for accurate photometry. Thus, in summary, all 323 galaxies in the HRS have been observed at 160 μm , whereas 100 μm data are available for 322 objects.

All raw PACS data were processed from Level-0 to Level-1 within HIPE (v10.0.0, Ott 2010) using the calibration file v48. This pre-processing includes, among the other tasks, pixel flagging, flux density conversion and coordinate assignment. To remove the $1/f$ noise which, at this point, still dominates the timelines, the Level-1 data were fed into *Scanamorphos* (version 21, Roussel 2013), an IDL algorithm which performs an optimal correction by exploiting the redundancy in the observations of each sky pixel. No noise modelling is hence needed. The pixel size of the final maps was chosen to sample at the best the point-spread-function, at the respective wavelengths, typical of the data taken at medium scan speed: 1.7 and 2.85 arcsec pixel⁻¹ at 100 and 160 μm , respectively (i.e., FWHM/4). The typical pixel-by-pixel noise in the map varies between ~ 0.1 and ~ 0.25 mJy pixel⁻¹ at 160 μm and between ~ 0.04 and ~ 0.1 mJy pixel⁻¹ at 100 μm .

In order to show the data quality of the new observations presented here, in Fig. 1 we compare the PACS images for three of our targets with the RGB Sloan Digital Sky Survey (Abazajian et al. 2009) optical and SPIRE 250 μm (Ciesla et al. 2012) images. We show an example of an early-type galaxy with dust lanes (HRS45, top row), late-

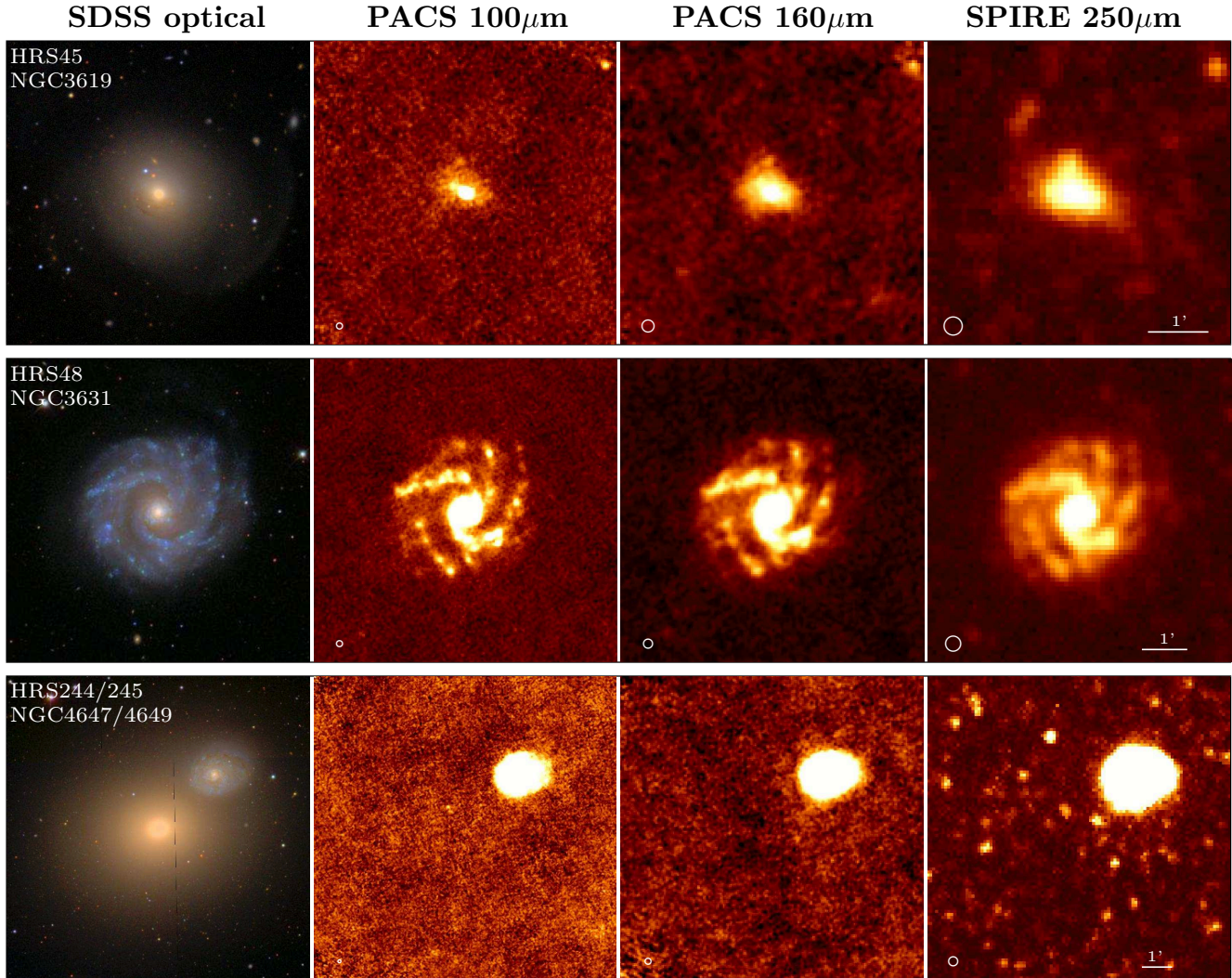


Figure 1. Comparison of the quality of our PACS images with the Sloan Digital Sky Survey optical and SPIRE 250 μm images. We show three types of objects: an early-type with dust lanes (top row), an unperturbed late-type spiral and an un-detected elliptical and its spiral companion. The size of the PACS and SPIRE beams is shown in the bottom left corner of each panel.

type galaxy (HRS48, middle row) and un-detected elliptical and its spiral companion (HRS244/245, bottom row).

2.3 PACS 100 and 160 μm integrated photometry

Integrated 100 and 160 μm photometry has been performed following very closely the technique used by Ciesla et al. (2012) for the SPIRE data of HRS galaxies. This is crucial to properly combine the two datasets, and to characterise the shape of the SED across the entire 100–500 μm wavelength range. Thus, whenever possible, we determined integrated flux densities within the same apertures adopted in Ciesla et al. (2012). The aperture sizes are adapted to include the entire extent of the FIR emission from the galaxies, and they correspond to ~ 1.4 , ~ 0.7 and ~ 0.3 times the optical diameter for late-type, lenticular and elliptical galaxies, respectively. Only for 36 galaxies ($\sim 11\%$ of the sample) we choose different sizes than those used for SPIRE. There are three different reasons why we did so: a) For 23 galaxies (HRS6, 14, 22, 32, 67, 71, 75, 158, 209, 223, 225, 238, 243,

249, 255, 257, 261, 264, 286, 300, 315, 317, 322) the 100 and 160 μm emission is significantly less extended than the size of the aperture used by Ciesla et al. (2012). Although this does not affect the estimate of the integrated flux density, it artificially boosts the error associated with our measurements to values always above 50%, and sometimes even higher than 100%. Thus, for these objects, we reduced the size of the aperture (on average by $\sim 26\%$) to obtain more realistic error estimates. We note that the size chosen is still larger than the extent of the FIR emission (so that aperture corrections are not necessary), and that the flux density estimated within these new apertures is consistent with the value obtained using Ciesla et al. (2012) apertures. b) 10 galaxies (HRS7, 68, 129, 138, 161, 174, 210, 231, 258, 308) were not spatially resolved in the SPIRE bands, and SPIRE photometry was carried out directly on the time-line data. For these cases, which are generally resolved by PACS, we chose new apertures which include all the emission from the target. c) For 3 galaxies (HRS4, 122, 263), the PACS maps available from the archive were slightly smaller than our

SPIRE maps. While these maps are large enough to include the entire aperture used in Ciesla et al. (2012), no space is left to properly estimate the background. Thus, the aperture has been reduced in order to allow a more accurate background estimate, and still encompass all the emission from the galaxy.

Sky background was determined in fifteen to thirty regions, depending on the size of the target, around the chosen aperture. The use of various regions instead of just a circular annulus makes it easier to estimate the large scale variations in the background and to avoid background/foreground sources around the target. The mean sky value was then subtracted from each map before performing the flux density extraction. Since cirrus contamination is significantly less of an issue than in SPIRE images, we did not find necessary to perform a more complex modelling of the background. However, as discussed below, the effect of any residual large scale gradient is included in our error estimates.

Errors on integrated flux densities have been estimated following the guidelines described in Roussel (2013), which are consistent with what is done in Ciesla et al. (2012) for HRS SPIRE data. Briefly, there are three sources of errors that affect our measurements:

$$\sigma_{tot} = \sqrt{\sigma_{cal}^2 + \sigma_{instr}^2 + \sigma_{sky}^2} \quad (2)$$

where σ_{cal} is the flux calibration uncertainty (here assumed to be 5%; Balog et al. 2013), σ_{instr} is the instrumental noise which depends on the number of scans crossing a pixel, and is obtained by summing in quadrature the values on the error map within the chosen aperture, and σ_{sky} is the error on the sky measurement. As discussed in Roussel (2013), the sky uncertainty results from the combination of the uncorrelated error on the mean value of the sky (σ_{skypix} i.e., the pixel-to-pixel variation across the image), and the correlated noise due to long time-scale drift residuals responsible for the large scale structures present in the image background ($\sigma_{skymean}$ i.e., the standard deviation of the mean value of the sky measured in different apertures around the galaxy; see also Boselli et al. 2003; Gil de Paz & Madore 2005). In detail,

$$\sigma_{sky} = \sqrt{N_{ap}\sigma_{skypix}^2 + N_{ap}^2\sigma_{skymean}^2} \quad (3)$$

where N_{ap} is the number of pixels in the aperture used to integrate the galaxy flux density. As expected, for the vast majority of our objects the dominant source of error is the correlated uncertainty on the large-scale structure of the background. The average total uncertainties are $\sigma_{tot} \sim 16\%$ and 12% at 100 and $160 \mu\text{m}$, respectively.

Out of the 323 galaxies observed, 282 have been detected in both bands (284 at $160 \mu\text{m}$ only). This matches the HRS detection fraction in the SPIRE bands (i.e., 284 galaxies detected at $250 \mu\text{m}$), allowing us to characterise the shape of the FIR/sub-mm SED across the entire $100\text{--}500 \mu\text{m}$ range for almost 300 galaxies. In case of non detections, upper limits have been estimated as $3 \times \sigma_{tot}$, using the same apertures as in Ciesla et al. (2012).

The results of our photometry are presented in Table 1. The columns are as follows:

Columns 1-6: HRS (Boselli et al. 2010b), CGCG (Zwicky et al. 1961), VCC (Binggeli et al. 1985), UGC (Nilson 1973), NGC (Dreyer 1888) and IC (Dreyer 1895) names.

Columns 7-8: the J2000 right ascension and declination.

Column 9: Morphological type, taken from Cortese et al. (2012a): -2=dE/dS0, 0=E-E/S0, 1=S0, 2=S0a-S0/Sa, 3=Sa, 4=Sab, 5=Sb, 6=Sbc, 7=Sc, 8=Scd, 9=Sd, 10=Sdm-Sd/Sm, 11=Sm, 12=Im, 13=Pec, 14=S/BCD, 15=Sm/BCD, 16=Im/BCD, 17=BCD.

Column 10: $100 \mu\text{m}$ flux density measurement flag. Non detections=0, Detections=1, Confused (i.e., flux density estimate significantly contaminated by the presence of another object)=2. For confused galaxies, flux densities should be considered as an upper limit to the real value.

Column 11: Integrated $100 \mu\text{m}$ flux density, or upper limit in Jy.

Column 12: Total uncertainty on the $100 \mu\text{m}$ flux density measurement in Jy.

Column 13: $160 \mu\text{m}$ flux density measurement flag.

Column 14: Integrated $160 \mu\text{m}$ flux density, or upper limit in Jy.

Column 15: Total uncertainty on the $160 \mu\text{m}$ flux density measurement in Jy.

Columns 16-18: Major, minor semi-axis (in arcseconds) and position angle (in degrees) of the aperture used for the photometry.

Column 19: *Herschel* Proposal ID.

This table, as well as all the reduced PACS maps, are publicly available on the Herschel Database in Marseille (HeDaM, <http://hedam.oamp.fr/>).

2.4 Comparison with the literature

In order to check the reliability of the PACS flux density measurements presented here, we compare our far-infrared integrated flux densities with the values presented in the literature, which are based on PACS, *Spitzer*/MIPS or IRAS observations. The results of these comparisons are shown in Fig. 2.

The difference between our flux density estimates and those presented in Dale et al. (2012) is $\sim +6\%$ (standard deviation of $\sim 2\text{--}3\%$), with our flux densities being brighter, although the number statistics is very small (6 galaxies in total). This difference is within the quoted uncertainties, and is mainly due to the different technique used to estimate flux densities (i.e., different background apertures and the use of aperture corrections not adopted in this work).

Auld et al. (2013) recently published PACS flux density measurements for all the VCC galaxies in the HeViCS footprint. A comparison between the flux density estimates for the 65 detected galaxies in common reveals a nice correlation between the two estimates with a standard deviation of just $\sim 12\%$ and $\sim 7\%$ at 100 and $160 \mu\text{m}$, respectively. However, Auld et al. (2013) measurements are systematically $\sim 12\%$ and $\sim 15\%$ lower than ours.

After various tests, we concluded that there are two main reasons for this discrepancy. First, a different flux density estimate technique. Auld et al. (2013) used apertures on average significantly smaller than ours (e.g., see their Fig. 3), and then applied aperture corrections. Indeed, by using our own apertures on the Auld et al. (2013) dataset, we find no systematic offset with our $100 \mu\text{m}$ data, whereas at $160 \mu\text{m}$ there is still a difference of $\sim 12\%$.

Second, a different data reduction technique. Auld et al. (2013) used the *naive* projection task `photProject` in HIPE

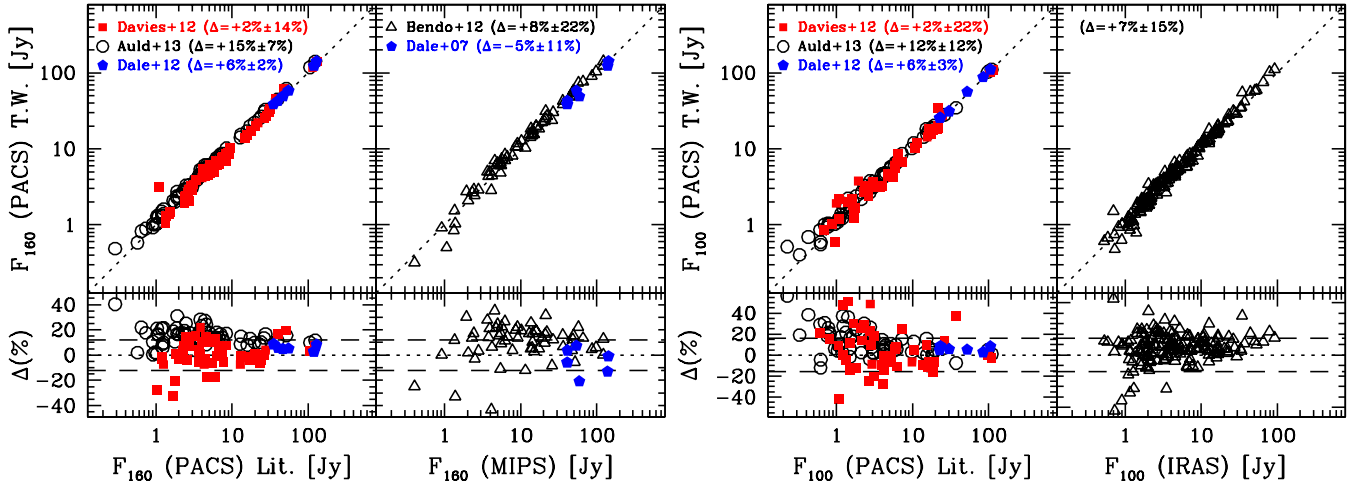


Figure 2. Comparison between our 160 μm (left) and 100 μm (right) flux density estimates and those presented in the literature. The bottom panels show the difference (this work (T.W.) - literature) in percentage for each dataset. For each PACS channel, the left panel shows the comparison with literature estimates based on PACS data, while in the right panel the comparison with *Spitzer*/MIPS and IRAS observations is presented. The dotted lines indicate the one-to-one relation, and the dashed lines the average uncertainty in our flux density estimates.

to reduce PACS images. This requires the use of a high-pass filter to correct for $1/f$ noise, and such procedure could remove diffuse emission associated to extended objects. By using the same apertures on the HeViCS maps reduced with both `photProject` and `Scanamorphos`, we find that `photProject` maps provide flux densities $\sim 10\%$ lower than those obtained with `Scanamorphos`, while no difference is seen at 100 μm . Thus, the remaining difference at 160 μm is due to the use of `photProject` instead of `Scanamorphos`. Indeed, as mentioned above, this is likely due to the use of high-pass filtering which removes diffuse emission, much more commonly present at 160 μm than at 100 μm (see also Rémy-Ruyer et al. 2013).

We also compared our measurements to those presented by Davies et al. (2012) for the 49 galaxies in common. These are based on an early HeViCS data release and are measured on apertures much more similar to the ones we used. Our flux density measurements agree very well with these estimates ($\sim +2 \pm 22\%$ and $\sim +2 \pm 14\%$ at 100 and 160 μm , respectively). The scatter is larger than in the case of Auld et al. (2013), but consistent with the typical uncertainty given in Davies et al. (2012). It is likely that, in this case, the different calibration between the two datasets compensates for the intrinsic differences between `photProject` and `Scanamorphos`, providing a set of measurements consistent with our own.

Spitzer/MIPS 160 μm flux densities for 103 galaxies in the HRS have been published by Bendo et al. (2012). In order to perform a proper comparison with our data, we removed those galaxies which were flagged as problematic due to incomplete coverage, or simply being confused with other nearby galaxies of similar surface brightness in Bendo et al. (2012). For the remaining 65 objects in common our flux densities are $\sim 8\%$ brighter than those of MIPS one, with quite a large scatter ($\sim 22\%$). This large scatter is mainly due to two galaxies (which fall outside the residual plot in Fig. 2):

HRS129, 258. A comparison between the PACS, SPIRE and MIPS data for these galaxies shows that the MIPS data suffer from background confusion effects, making it difficult to separate emission from the target and background sources. Moreover, the MIPS observations for these galaxies were performed in photometry mode, which produces compact maps where it is difficult to measure the background. Once these are removed from the sample, the difference between MIPS and PACS measurements becomes $\sim +10 \pm 14\%$. Conversely, the comparison with the *Spitzer*/MIPS 160 μm flux densities presented in Dale et al. (2007) for the 6 SINGS galaxies in our sample shows an average difference of $\sim -5 \pm 11\%$. All these values are within the 12% flux calibration uncertainty in MIPS data (Stansberry et al. 2007). A PACS-to-MIPS 160 μm flux density ratio systematically higher than 1 has also been found by comparing pixel-by-pixel photometry of nearby galaxies (Aniano et al. 2012; Draine et al. 2013).

We can thus conclude that our 160 μm PACS flux density measurements are consistent with those of *Spitzer*/MIPS within $\sim 20\%$, in agreement with the results obtained by the PACS Team (Paladini et al. 2012).

Finally, we compared our PACS 100 μm flux density estimates with those presented in the IRAS Faint Source Catalogue (164 galaxies after exclusion of confused/contaminated objects), finding an average difference of $\sim +7 \pm 15\%$ (see also Ali 2011).

We remind the reader that, although the central wavelengths of MIPS and IRAS correspond to those of PACS, the bandpasses are not identical and part of the offsets shown above are certainly due to the different filter responses of the three instruments.

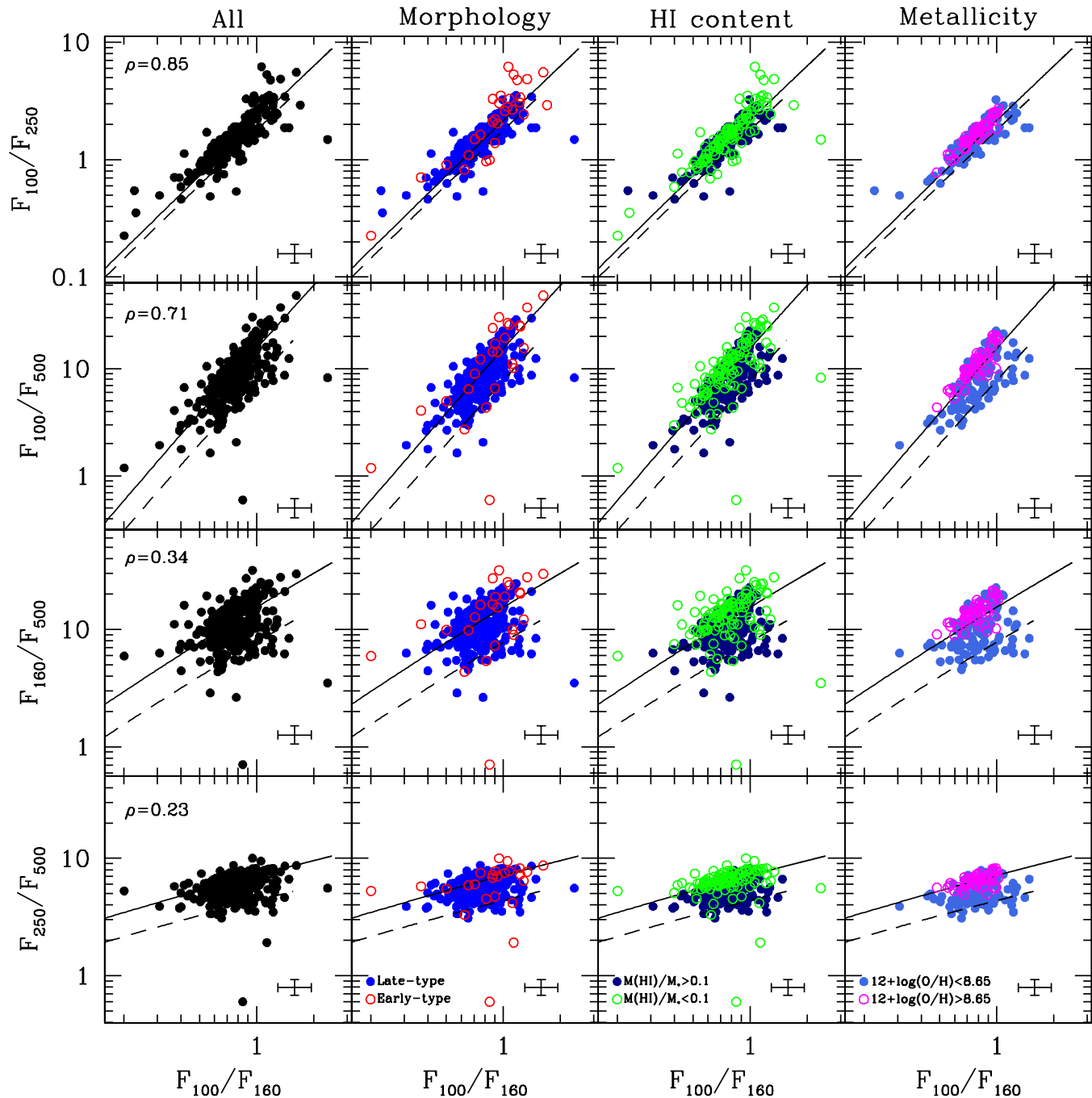


Figure 3. From top to bottom: 100-to-250 μm , 100-to-500 μm , 160-to-500 μm and 250-to-500 μm as a function of the 100-to-160 μm flux density ratio. The first column shows the entire HRS sample, while in the following three columns points are colour-coded according to morphological type (open circles=E+S0, filled circles=Sa and later), HI gas fraction (open circles= $\log(M(\text{HI})/M_*) < -1$, filled circles= $\log(M(\text{HI})/M_*) > -1$) and gas phase metallicity (open circles= $12 + \log(\text{O}/\text{H}) > 8.65$, filled circles= $12 + \log(\text{O}/\text{H}) < 8.65$). The Pearson correlation coefficients (ρ) for the whole sample are shown in the top left corner of each panel. The solid and dashed lines represent the expected colours for a modified black body with $\beta=2$ and 1, respectively. We consider a temperature range between 10 and 40 K. Typical errorbars are shown on the bottom right corner of each panel.

3 FAR-INFRARED/SUB-MILLIMETER COLOURS AS A PROXY FOR THE SHAPE OF THE DUST SED

In the last few years, several studies have shown how infrared colours can be used as a proxy of dust properties (e.g., Boselli et al. 2010a, 2012; Dale et al. 2012; Bendo et al.

2010, 2012; Galametz et al. 2010; Boquien et al. 2011; Rémy-Ruyer et al. 2013). The novelty of the present work is that, for the first time, we cover the 100-500 μm domain for a representative sample of galaxies spanning a large range in stellar mass, star formation activity, cold gas and metal content. For example, compared to the work pre-

Table 2. The Pearson correlation coefficients (ρ) and scatter (σ) of the best-fitting bisector linear fit for each sample shown in the colour-colour relations of Fig. 3.

<i>Sample</i>	$F_{100}/F_{160} - F_{100}/F_{250}$			$F_{100}/F_{160} - F_{100}/F_{500}$			$F_{100}/F_{160} - F_{160}/F_{500}$			$F_{100}/F_{160} - F_{250}/F_{500}$		
	<i>N</i>	ρ	σ	<i>N</i>	ρ	σ	<i>N</i>	ρ	σ	<i>N</i>	ρ	σ
<i>All</i>	282	0.84	0.05	274	0.70	0.10	274	0.30	0.14	274	0.23	0.12
<i>Early - type</i>	29	0.88	0.09	25	0.71	0.17	25	0.39	0.23	25	0.14	0.14
<i>Late - type</i>	253	0.83	0.05	249	0.69	0.10	249	0.27	0.14	249	0.28	0.12
$M(HI)/M_{\odot} < 0.1$	106	0.84	0.04	101	0.68	0.06	101	0.26	0.09	101	0.13	0.10
$M(HI)/M_{\odot} > 0.1$	169	0.84	0.06	167	0.71	0.11	167	0.34	0.15	167	0.34	0.11
$12 + \log(O/H) > 8.65$	50	0.95	0.02	50	0.88	0.03	50	0.66	0.05	50	0.53	0.05
$12 + \log(O/H) < 8.65$	112	0.86	0.06	110	0.73	0.11	110	0.32	0.15	110	0.33	0.10

sented in Boselli et al. (2012), which focused on HI-normal spiral galaxies only, this analysis takes advantage of a more complete coverage at wavelengths shorter than 250 μm , and includes the entire HRS sample detected by *Herschel* (282 versus 146 objects). Similarly, the number of HRS galaxies detected at all PACS and SPIRE wavelengths is significantly larger (i.e., 282 versus 195) than that of Auld et al. (2013), which focuses on Virgo cluster galaxies only.

Particularly interesting is to quantify how well the shapes of the dust SED at the short and long wavelength-ends correlate among each other. Indeed if, in the 100-500 μm wavelength range, the dust SED can be well approximated by a single modified black-body with fixed β (i.e., the variation of the dust emissivity with frequency described by $\kappa_{\nu} = \kappa_0 \times (\nu/\nu_0)^{\beta}$), all FIR/sub-mm colours should be strongly correlated.

The SPIRE flux densities are obtained from Ciesla et al. (2012), but we applied several corrections to these flux estimates. We multiplied their values by 1.0253, 1.0250 and 1.0125 at 250, 350 and 500 μm to take into account the new SPIRE calibration (v.11), and then by 0.9097, 0.9136 and 0.8976 at 250, 350 and 500 μm , to correct for the new beam areas (Bendo et al. 2013; *Herschel* Space Observatory 2013). We did not make any attempt to include variations of the beam size as a function of the shape of the SED (*Herschel* Space Observatory 2013), as these are generally within the measurement errors ($\lesssim 10\%$). Moreover, such correction would mainly result in a systematic offset in the flux densities, whereas the relative variation between the SPIRE bands would be $\lesssim 3\%$ for the ranges of β investigated here. Thus, we are confident that this does not affect our conclusions.

In Fig. 3 we plot the 100-to-160 μm flux density ratio, which usually embraces the peak of the dust SED, as a function of various flux density ratios (i.e., from top to bottom: 100-to-250 μm , 100-to-500 μm , 160-to-500 μm and 250-to-500 μm) sensible to the shape of the SED at increasingly longer wavelengths². Similar results are found if additional colours (e.g., including the 350 μm flux density) are used.

It is clear that the farther away in wavelength two colours are, the weaker their correlation is, as already noted by Boselli et al. (2012). Indeed, the Pearson correlation co-

efficient (ρ) decreases from ~ 0.8 to ~ 0.2 when moving from the 100-to-250 μm to the 250-to-500 μm flux density ratios (see first column of Fig. 3). Intriguingly, the increase of a factor of ~ 3 in scatter (σ)³ observed when moving from the top to the third panel appears to be due to a population of galaxies that detaches from the main relation. To see if this is indeed the case, in Fig. 3 we highlight galaxies according to (from left to right) their morphological type, the ratio of their atomic cold gas (HI) to stellar mass content and gas-phase metallicity. HI measurements have mainly been obtained from Haynes et al. (2011) and Springob et al. (2005), and are presented in Boselli et al. (2014)⁴. Stellar masses are from Cortese et al. (2012a), and gas-phase metallicities (i.e., oxygen abundances) converted into the Pettini & Pagel (2004) O3N2 base metallicity are taken from Hughes et al. (2013). We use $12 + \log(O/H) = 8.65$ (above which the stellar vs. mass metallicity relation starts flattening, Kewley & Ellison 2008) and $M(HI)/M_* = 0.1$ (below which the stellar mass vs. HI fraction relation is no longer linear, Cortese et al. 2011; Bothwell et al. 2009) to divide gas-rich/metal-poor from gas-poor/metal-rich galaxies. The Pearson correlation coefficients and scatter around the best-fitting bisector linear fit are indicated in Table 2.

Gas-rich/metal-poor galaxies seem to be responsible for the significant increase in scatter when moving from the 100-to-250 μm to the 160-to-500 μm colour-colour plots. If we consider gas-poor/metal-rich galaxies only, the scatter in the three bottom panels of Fig. 3 decreases by at least a factor ~ 2 . Indeed, performing a Kolmogorov-Smirnov test, we found that there is only a $\sim 4\%$ chance that the 160-to-500 μm colour distributions of metal-poor ($12 + \log(O/H) < 8.65$) and metal-rich ($12 + \log(O/H) > 8.65$) galaxies are drawn from the same population, as already demonstrated by Boselli et al. (2012). We note that some galaxies do not appear in the third and fourth column of Fig. 3. This is because for some objects HI and metallicity information is not available.

Our findings suggest that, in the 100-500 μm regime, the shape of the dust SED for galaxies with stellar mass

² In order to avoid the need to apply colour corrections when comparing with model predictions, here we plot the ratio of the responsivity function-weighted flux density measurements.

³ In order to minimize the effect of outlier galaxies, the scatter is defined as the interquartile of the distribution of perpendicular distances from the best-fitting bisector linear fit for each sample.

⁴ This is an updated version of the values presented in Cortese et al. (2011, 2012b), which takes advantage of the recently published ALFALFA flux densities (Haynes et al. 2011) for a considerable fraction of the HRS footprint.

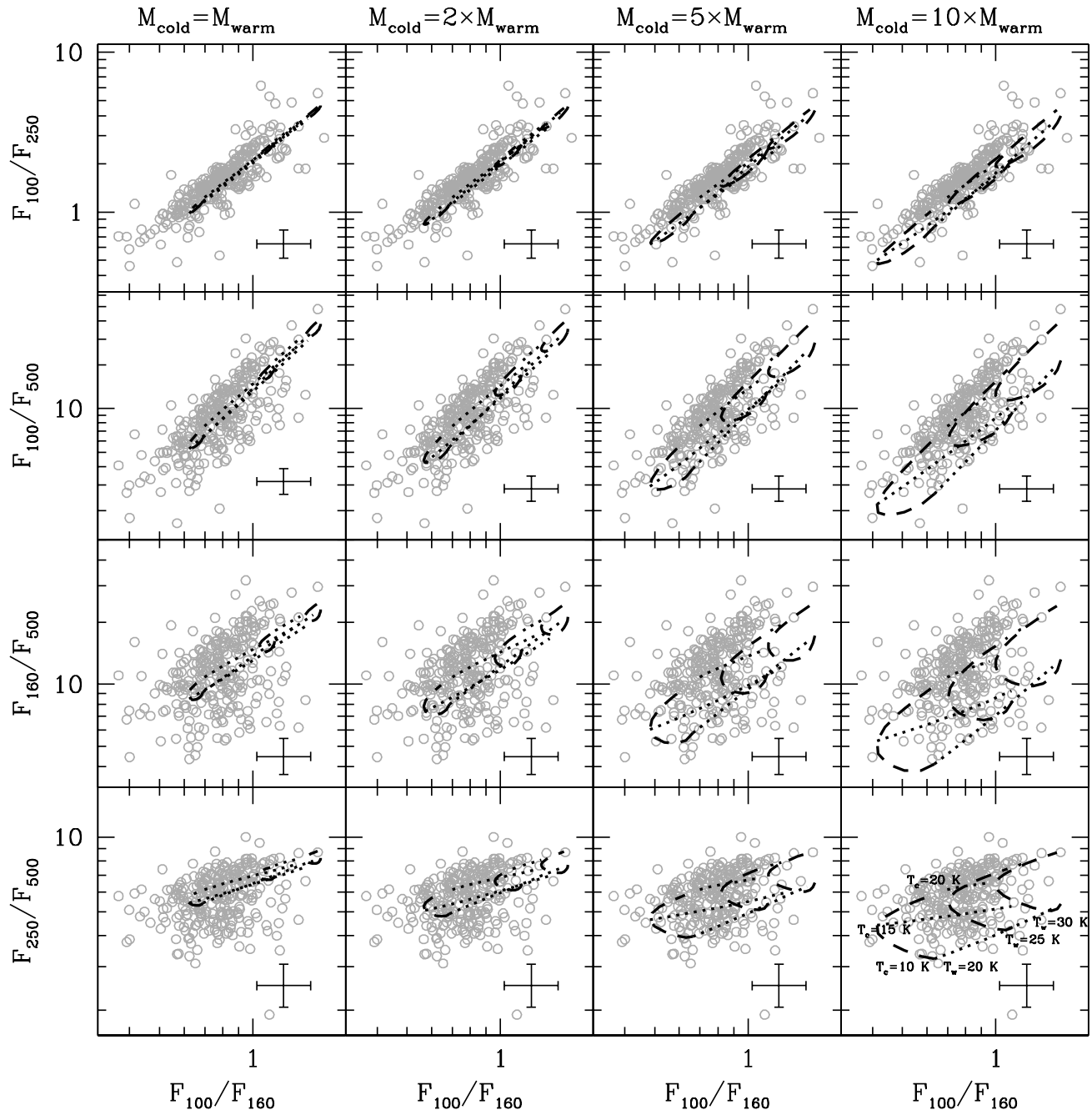


Figure 4. Same as Fig. 3, but with the predictions for two temperatures modified black-body SEDs with $\beta=2$ overplotted on the data points. In each plot, isotherms for the cold ($T_c=10, 15$ and 20 K) and warm ($T_w=20, 25$ and 30 K) dust components are indicated by the dotted and dashed lines, respectively. Cold-to-warm dust mass ratios are 1, 2, 5 and 10 from left to right.

$10^8 \lesssim M_*/M_\odot \lesssim 10^{12}$ cannot be reproduced by simply varying the value of the average dust temperature. In other words, either β must also vary (Boselli et al. 2012; Smith et al. 2012; Rémy-Ruyer et al. 2013) or multiple temperatures components are required (Shetty et al. 2009; Dunne & Eales 2001; Boquien et al. 2011; Bendo et al. 2012; Clemens et al. 2013).

In order to visually illustrate this result, we plot in Fig. 3 and 4 the colours expected for these two different

scenarios. In Fig. 3 we show the flux density ratios derived from single modified black-bodies with temperatures ranging from 10 and 40 K and β values fixed to 2 (solid line) and 1 (dashed line). In Fig. 4, we show a combination of two modified black-bodies with $\beta=2$. We vary the cold dust temperature (T_c) from 10 to 20 K, and the warm dust temperature (T_w) from 20 to 30 K. The four columns show different mass ratios M_{cold}/M_{warm} increasing from 1 (left) to 10 (right).

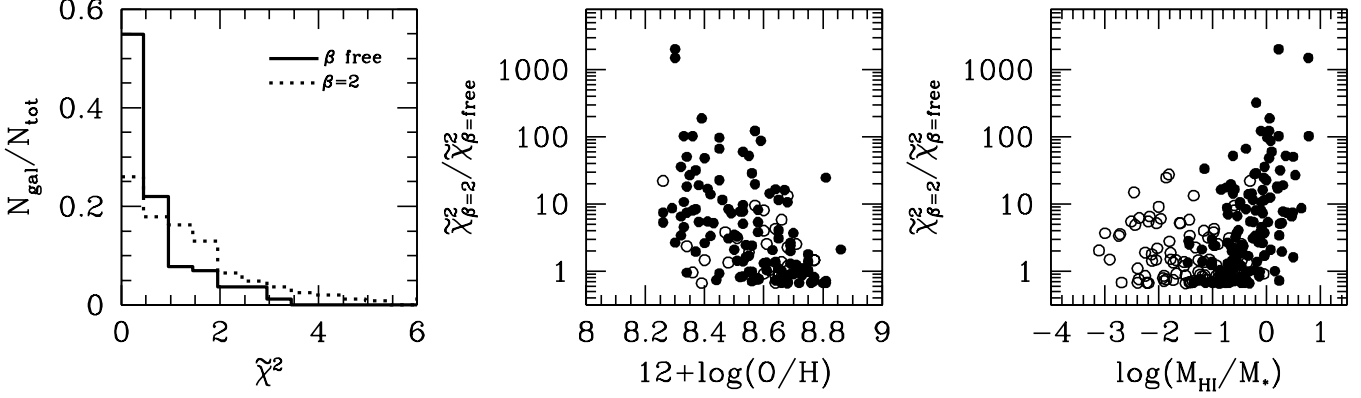


Figure 5. The left panel shows the distribution of reduced χ^2 ($\bar{\chi}^2$) for the best-fitting single modified black-body with β =free (solid line) and $\beta=2$ (dashed). The ratio of χ^2 obtained for the two cases as a function of gas-phase metallicity and HI gas fraction are presented in the central and right panel, respectively. Empty circles show galaxies with HI deficiency greater than 0.5. We show only those galaxies for which at least one of the two χ^2 corresponds to a probability $P \geq 95\%$.

It is clear that, while the temperature is the main driver of the trends observed in each colour-colour plot, only a variation in β , or an additional temperature component, can explain the increasing scatter when moving from the 100-to-250 μm to 160-to-500 μm colours. Interestingly, the two temperature components scenario is able to reproduce the observed range of colours only if the warm component contributes negligibly to the total dust budget of the galaxy (i.e., $M_{\text{cold}}/M_{\text{warm}} \gtrsim 5$; Vlahakis et al. 2005). This is easy to understand if we consider the fact that, at fixed dust mass, the flux density emitted by a black-body in the FIR/submm wavelength range increases with temperature. Thus, if the warm and cold components have the same dust mass, the warm dust dominates the total emission, and the shape of the SED is very close to that of a single black-body. Only if the cold dust component dominates the mass budget, the shape of the combined SED deviates significantly from a single black-body.

Unfortunately, with our current data it is impossible to discriminate between a varying β and a multiple temperature component scenario. Our lack of coverage below 100 μm makes it meaningless to perform a two temperatures fit, as the warm component is not constrained. Thus, in the rest of this paper we will focus on the single modified black-body case only, and investigate how different assumptions on β can affect the interpretation of *Herschel* observations. A detailed comparison with the predictions of the Draine et al. (2007) dust models will be presented in a forthcoming paper (Ciesla et al., submitted.).

4 FITTING THE DUST SED WITH A SINGLE MODIFIED BLACK-BODY

4.1 How well do colours trace the average dust temperature?

The results presented in the previous section show that FIR/sub-mm colours may not always represent a proxy for the average underlying dust temperature. In order to investigate this issue in more detail, it is interesting to quantify how the FIR/sub-mm colours correlate with the parameters

obtained from a single modified black-body fitting. We assume either a constant value of $\beta=2$, or keep this as a free parameter. The model functions were convolved with the PACS and SPIRE filter response functions and fitted to the relative spectral responsivity function-weighted flux density measurements. Best-fit parameters and their 1σ uncertainties are determined via a χ^2 minimisation using the Python version of the minimisation library MINUIT (James & Roos 1975). We choose $\beta=2$ simply because this seems to correctly reproduce the shape of the SED for massive, metal-rich spiral galaxies in the local Universe (Davies et al. 2012; Boselli et al. 2012; Draine et al. 2013). However, our results do not qualitatively change if a different (but fixed) value of β is used. In the rest of the paper, we consider only those objects detected in all 5 PACS/SPIRE bands, and for which the reduced χ^2 ($\bar{\chi}^2$) corresponds to a probability $P \geq 95\%$: i.e., $\bar{\chi}^2_{\text{dof}=3} < 2.6$ (203 galaxies) and $\bar{\chi}^2_{\text{dof}=2} < 3$ (242 galaxies) for a fixed and variable β , respectively. The best-fit dust masses and temperatures for these galaxies, as well as their distance, are provided in Table 3. This guarantees that we are not contaminated by objects whose FIR/submm emission is dominated by synchrotron emission (Baes et al. 2010).

A comparison between the reduced χ^2 obtained for the β =free and $\beta=2$ cases is shown in Fig. 5. Not surprisingly, leaving β free provides on average better fits. Moreover, as shown in the central and right panel of Fig. 5, the difference between the two techniques increases when moving towards metal-poor/gas-rich systems. This is even more evident when HI-deficient galaxies (i.e., $Def_{\text{HI}} > 0.5$, empty points in Fig. 5), for which the gas content is no longer a good indicator of enrichment history (Cortese & Hughes 2009; Hughes et al. 2013), are excluded ($\rho = 0.38$ and 0.54 for all galaxies and HI-normal systems only, respectively).

In Fig. 6, we show how the FIR/sub-mm colours correlate with the best-fit parameters obtained from our SED fitting. Not surprisingly, all SPIRE and PACS colours strongly correlate with dust temperature if β is kept fixed (we note that these results do not qualitatively change if we fix β to a different value). It is also expected that the lowest scatter is observed for the colour spanning the largest wavelength range (i.e., the 100-to-500 μm flux density ratio), as the vari-

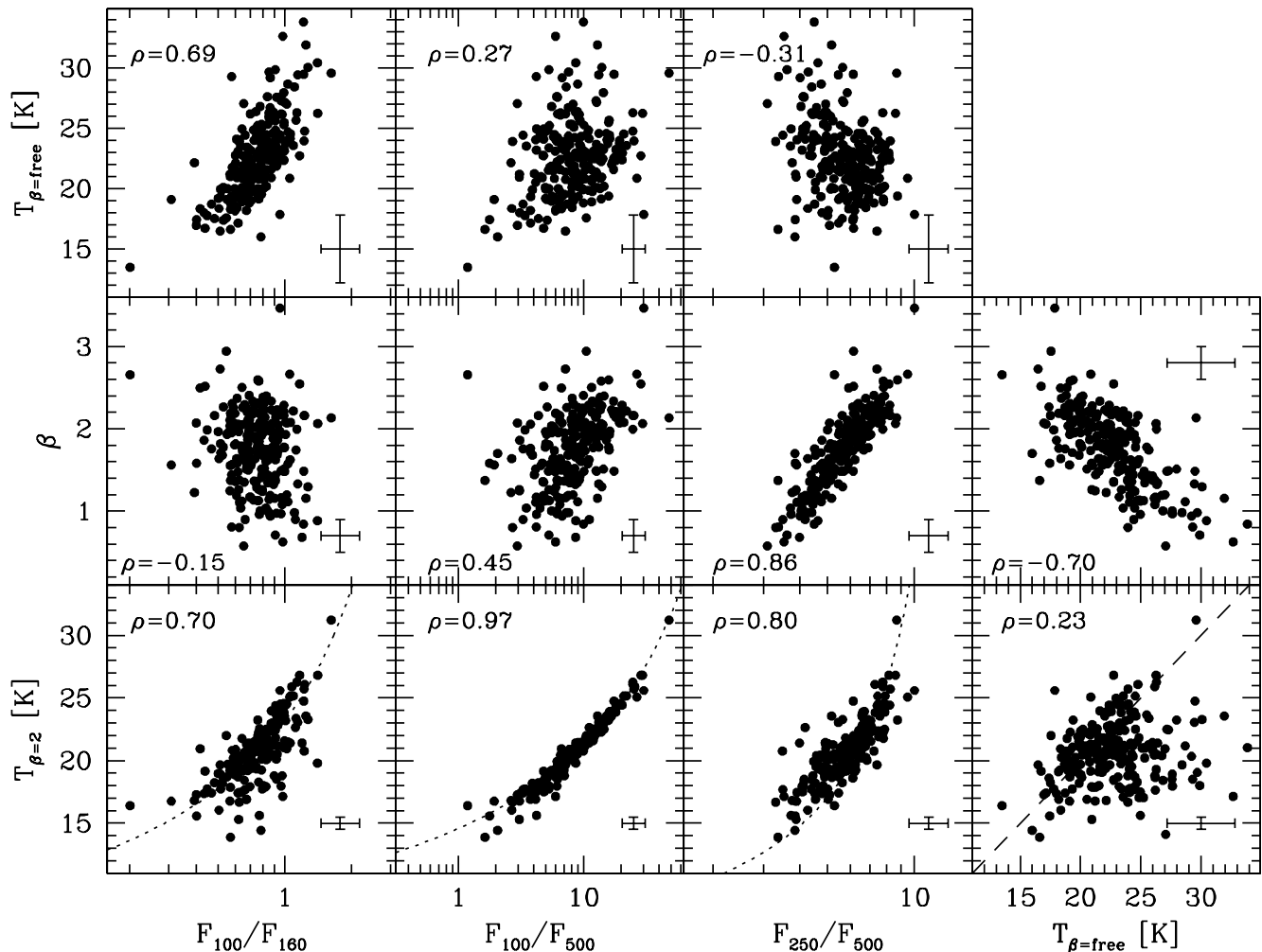


Figure 6. The modified black-body best-fitting parameters as a function of far-infrared/sub-millimeter colours (from left to right: 100-to-160 μm , 100-to-250 μm , 100-to-500 μm and 250-to-500 μm flux density ratio). The bottom row shows the dust temperature obtained by keeping β fixed to 2, while the middle and top rows show the best-fitting values for β and T obtained by varying both parameters freely. The Pearson correlation coefficients are indicated in each panel. In the bottom row, the dotted lines show the expected relations between temperature and colour for a single modified black-body with $\beta=2$, while the dashed line indicates the 1-to-1 relation.

ation in colour is larger, and less affected by measurement errors.

More interesting is the case when β is treated as a free parameter. In this case, there is a clear difference in the colours behaviour when crossing a λ of $\sim 200 \mu\text{m}$. At shorter wavelengths, there is still a strong correlation of colour with temperature ($\rho \sim 0.7$), while only a very weak trend is seen with β ($\rho \sim 0.15$). Moving to longer wavelengths, the trends with temperature become weaker, and reverse for the 250-to-500 μm colour ($\rho \sim 0.3$), whereas the correlation with β becomes gradually stronger. The best relation is found with the 250-to-500 μm flux density ratio ($\rho \sim 0.9$), which appears to be mainly tracing variations of β and not dust temperature, as also shown in Fig. 3. These results are likely a direct consequence of the fact that the FIR/submm SED for our sample peaks at $\lambda < 200 \mu\text{m}$, and while the PACS colours trace the peak of the dust SED, any variations in the emissivity of the grains will predominantly affect the SPIRE colours. The average value of β for HRS galaxies is $\sim 1.8 \pm 0.5$, a value consistent with what is found in the Milky Way and

in other nearby galaxies (Planck Collaboration et al. 2013; Galametz et al. 2012; Boselli et al. 2012; Smith et al. 2012, 2013).

An important issue affecting any modified black-body χ^2 fitting with β and T as free parameters is the known anti-correlation between them, which is clearly shown in the right column of Fig. 6. While it is still debated whether part of this anti-correlation has a physical origin (Shetty et al. 2009; Galametz et al. 2012; Smith et al. 2012; Juvela & Ysard 2012; Juvela et al. 2013; Rémy-Ruyer et al. 2013; Tabatabaei et al. 2013), there is no doubt that it is mainly due to the χ^2 fitting technique (Shetty et al. 2009). Indeed, in the 2D β vs. T plane, the region corresponding to the absolute minimum of χ^2 depends on both quantities, giving rise to an anti-correlation between β and T . This is clearly visible by just looking at the 2D confidence levels for any χ^2 modified black-body fit. Since in the first and third columns of Fig. 6 temperature and β show opposite trends with colour, it is very likely that they are affected by this degeneracy. However, the significant difference in scatter be-

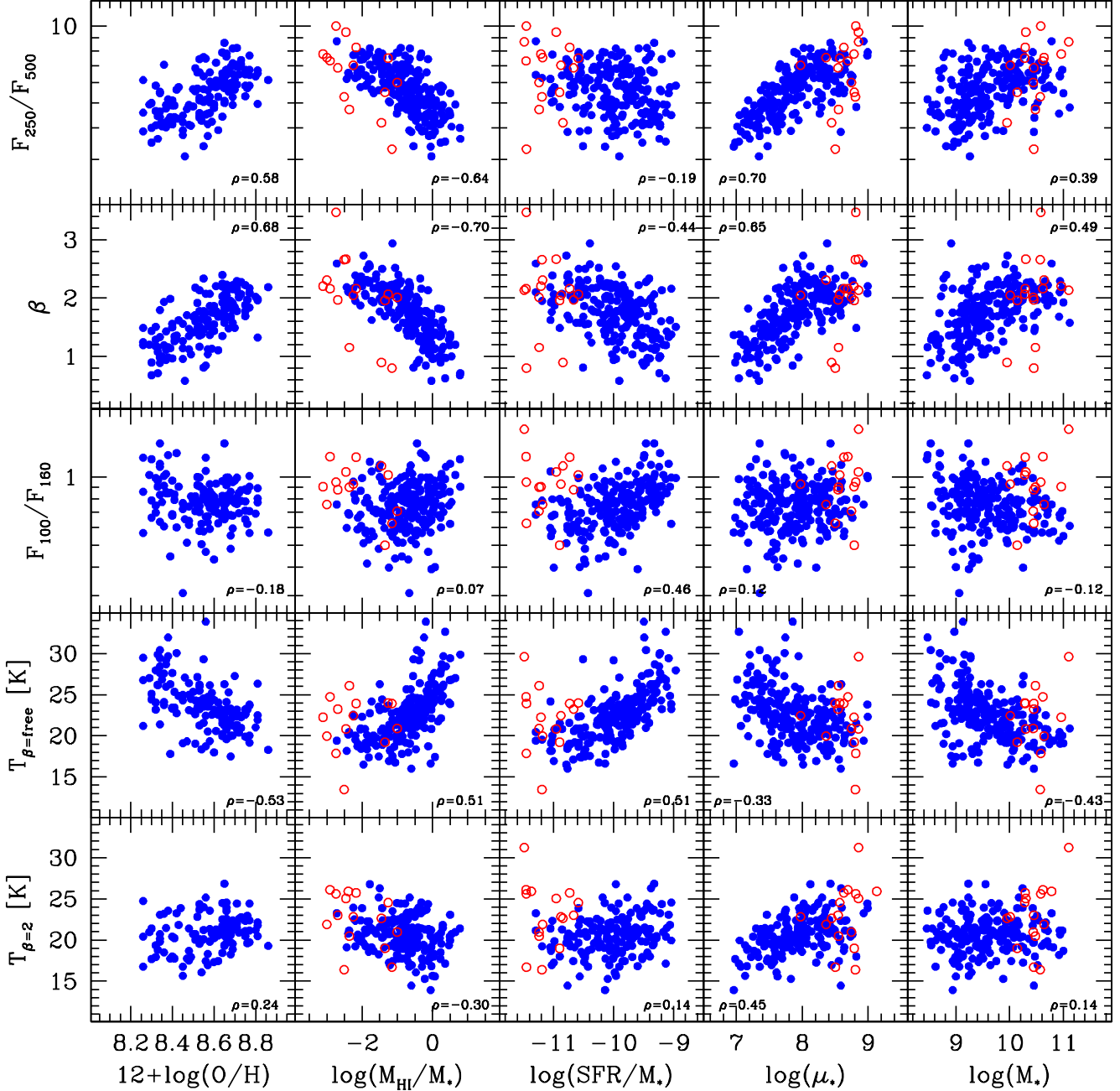


Figure 7. From top to bottom: the 250-to-500 μm flux density ratio, the best-fitting value of β , the 100-to-160 μm flux density ratio, the best fitting temperature assuming β =free and $\beta=2$ as a function of stellar mass, stellar mass surface density (μ_*), specific star formation rate (SFR/M_*), HI gas fraction (M_{HI}/M_*) and gas phase metallicity ($12+\log(\text{O}/\text{H})$). Filled and open circles show late- and early-type galaxies, respectively. The Pearson correlation coefficients for the whole sample are shown in each panel.

tween the various relations suggests that the 100-to-160 μm colour vs. T and 250-to-500 μm colour vs. β are less contaminated than the other correlations. As mentioned above, this is because the PACS colours mainly trace the peak of the dust SED, whereas the SPIRE ones are mostly sensitive to variations in the dust emissivity.

4.2 The relation between dust temperature, β and integrated galaxy properties

In this section we investigate further how the variation of β , necessary to reproduce the observed colours of HRS galaxies in a single modified black-body scenario, is mirrored by a variation in galaxy properties. For comparison, we will also show the results obtained by keeping β fixed, since we consider this an instructive exercise to illustrate how the model assumptions influence the parameters we derive. In Fig. 7, we show how the best-fitting dust parameters, as well as the

100-to-160 μm and 250-to-500 μm flux density ratios, are related to gas-phase metallicities, HI gas fractions, specific star formation rate (SFR/M_*), stellar mass surface density [$\mu_* = M_*/(2\pi R_{50,i}^2)$ where $R_{50,i}$ is the radius containing 50% of the total i -band light] and stellar mass. Star formation rates are determined by combining WISE 22 μm (Ciesla et al., submitted.) and NUV photometry (Cortese et al. 2012a) using the recipes presented in Hao et al. (2011) as described in Cortese (2012).

By comparing the two bottom rows of Fig. 7, it is clear that the assumptions made on β significantly influence the correlations between temperature and integrated galaxy properties. For β fixed to 2, the strongest correlation is found with stellar mass surface density ($\rho \sim 0.45$). A weak anti-correlation is visible with gas-fraction ($\rho \sim -0.3$), while no correlation is found with specific star formation rate, stellar mass or metallicity ($\rho \lesssim 0.2$). Quite different results are obtained if β is left free. In this case, the temperature anti-correlates very weakly with μ_* ($\rho \sim -0.3$), while it is strongly correlated with SFR/M_* (see also Clemens et al. 2013), HI gas fraction, metallicity and stellar mass ($\rho \sim 0.5$). Even more importantly, some of the correlations show opposite trends. For a fixed value of β , the temperature increases with metallicity and stellar mass surface densities, whereas it decreases for $\beta = \text{free}$. The ‘reversal’ of these correlations is driven exclusively by metal-poor/gas-rich galaxies, and it is simply a consequence of the fact that, for these objects, the best-fitting value of β is significantly lower than 2. Thus, many of the correlations shown in Fig. 7 depend on the assumptions made about the dust SED, and may not be physical (Magnelli et al. 2012; Roseboom et al. 2013).

In particular, we have shown (see Fig. 6) that the 100-to-160 μm and 250-to-500 μm flux density ratios are the best proxies for T and β , respectively. If all the trends observed in Fig. 7 are physical, we should find similar correlations when T and β are replaced by the flux density ratios. However, this is not always the case. The 100-to-160 μm flux density ratio correlates only with SFR/M_* ($\rho \sim 0.5$), while the 250-to-500 μm ratio correlates weakly with SFR/M_* ($\rho \sim -0.2$), but varies strongly with stellar mass, stellar mass surface density, HI gas fraction and gas-phase metallicity ($\rho \sim 0.6-0.7$). Thus, the T vs. HI gas fraction and β vs. SFR/M_* trends might be spurious.

In summary, our analysis confirms that the typical dust temperature of a galaxies as measured from a single modified black-body is mainly related to specific star formation rate, while β varies more with the degree of metal enrichment of the ISM. As discussed in the previous section, at this stage it is impossible to determine whether the variation of β across the HRS indicates a variation in the dust properties/composition, or it simply highlights the need of multiple temperature components for gas-rich/metal-poor/low-mass galaxies.

4.3 Dust mass estimates

It is interesting to investigate how the variation of β across the HRS for a single modified black-body affects the estimate of the dust mass reservoir. Thus, in the left panel of Fig. 8, we compare the dust masses obtained for $\beta = \text{free}$ and $\beta = 2$. Dust masses have been calculated from Eq. 1 assuming $\nu_0 = 856.5$ GHz (i.e., 350 μm) and $\kappa_0 = 0.192$ m²

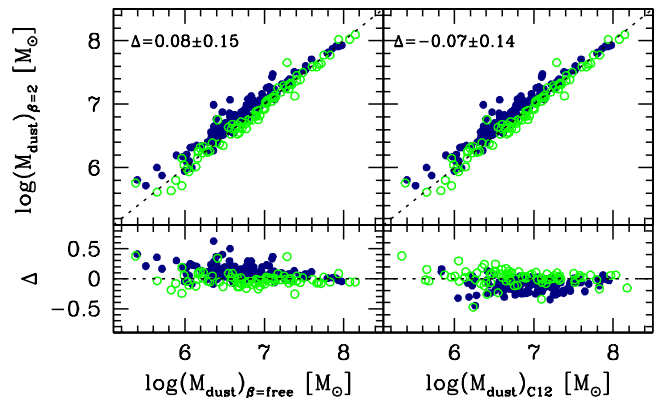


Figure 8. *Left panel:* Comparison between the dust masses obtained from a black-body SED fitting with $\beta = 2$ and $\beta = \text{free}$. *Right panel:* Dust masses obtained from a black-body SED fitting with $\beta = 2$ as a function of those obtained using the empirical recipes of Cortese et al. (2012b), which are based on SPIRE colours only. Filled and empty circles indicate gas-rich and gas-poor galaxies, respectively (see also Fig. 3).

kg⁻¹ (Draine 2003). It is evident that dust masses are significantly less affected than dust temperatures by the assumptions made on β . The average difference between the two measurements is ~ 0.08 dex, with a standard deviation of 0.15 dex, which is consistent with the typical statistical error obtained from the SED fitting: ~ 0.05 and 0.1 dex for $\beta = 2$ and $\beta = \text{free}$. Not surprisingly, the largest difference is observed in gas-rich galaxies (filled circles, $\Delta = 0.14 \pm 0.14$ dex), while the two techniques give consistent results for gas-poor systems (empty circles, $\Delta = -0.02 \pm 0.11$ dex).

This result implies that correlations involving dust masses are quite robust against the assumptions made on the shape of the SED. Different assumptions can certainly affect the exact slope of the dust scaling relations, but they are not able to produce the same dramatic inversion of some correlations observed for the dust temperature (see Fig. 7).

This conclusion is reinforced by the fact that the differences, already quite small, between the two cases might be overestimated, as we varied β , by keeping fixed the value of dust opacity κ_0 used to determine the dust mass. As recently shown by Bianchi (2013), this is not entirely correct because the value of κ_0 is calibrated on a dust model with a well defined value of β . Thus, if β changes, κ_0 should change as well. Unfortunately, varying κ along with β is far from trivial, and it is only possible by either having a consistent dust model for each value of β , or by comparing dust mass estimates obtained from SED fitting with the ones obtained from other independent methods: e.g., using the amount of cold gas and metals, as proposed by James et al. (2002).

Finally, it is interesting to compare the dust masses estimated by fitting a single modified black-body with $\beta = 2$, to those obtained by using the empirical recipes developed by Cortese et al. (2012b), which assume $\beta = 2$ but are based on SPIRE data only. In this way we can quantify the benefit provided by inclusion of the PACS data in the dust mass estimates. As shown in the right panel of Fig. 8, the two estimates show a good agreement with a mean difference of -0.07 dex and a standard deviation of 0.14 dex, lower than the typical uncertainty of 0.2 dex in the recipes by Cortese et al. (2012b). Even in this case, the largest offset

(-0.12 ± 0.11 dex) is found for gas-rich galaxies. This is a natural consequence of the fact that, for these objects, the shape of the dust SED is no longer perfectly consistent with $\beta=2$.

Thus, while dust mass estimates based on SPIRE colours are a reliable tool for estimating dust masses within 0.2 dex, only a complete coverage of the 100-500 μm wavelength range can provide us with accurate (within 0.1dex) dust mass estimates necessary to quantify in great detail the correlation between dust mass and other galaxy properties.

5 SUMMARY & CONCLUSIONS

In this paper we presented PACS 100 and 160 μm integrated photometry for the *Herschel* Reference Survey. We have combined these data with SPIRE observations to investigate how the shape of dust SED varies across the Hubble sequence. Being the largest representative sample of nearby galaxies with homogeneous coverage in the 100-500 μm wavelength domain, the HRS is ideal to quantify if and how dust emission varies across the local galaxy population. Our main results are as follows.

- The shape of the dust SED is not well described by a single modified black-body having just the dust temperature as a free parameter. Instead, there is a clear need to vary the dependence of the dust emissivity (β) on wavelength, or to invoke multiple temperature components in order to reproduce the colours observed in our sample. This is particularly important as the HRS does not include very metal-poor dwarf galaxies, for which we already knew that the dust SED is significantly different from the one of metal-rich, massive galaxies (Galliano et al. 2005, 2011; Engelbracht et al. 2008; Galametz et al. 2009; Rémy-Ruyer et al. 2013). Our results suggest that the difference in FIR/sub-mm colours between giant and dwarf galaxies (Draine & Li 2007) may not be the result of a dramatic transition in dust properties, but just the consequence of the gradual variation that we observe as a function of metal and gas content.

- The variation in the slope of the dust SED strongly affects dust temperature estimates from single modified black-bodies fits. In particular, the correlations between galaxy properties and dust temperatures strongly depend on the assumptions made on β : i.e., trends can disappear or even reverse. Conversely, dust mass estimates are more robust, and variations in β do not produce the same dramatic inversion of some correlations observed for the dust temperature.

- We confirm that the temperature of a single modified black-body is mainly related to specific star formation rate, while β varies more with the degree of metal enrichment of the ISM.

The results presented in this paper may appear in contradiction with several recent works showing that the dust SED is very well reproduced by a simple modified black-body with $\beta=2$ (Davies et al. 2012; Auld et al. 2013). However, all these works were focused on massive, metal-rich and relative gas-poor galaxies, for which we also find that a constant value of β provides a good fit to our data. It is when we move to the gas-rich/metal-poor regime that the shape of the SED starts to change (Boselli et al. 2010a, 2012; Rémy-Ruyer et al. 2013).

Our findings overall reinforce the results already presented in Boselli et al. (2010a, 2012). However, it is important to note that the discovery of a clear variation in the shape of the SED across the HRS has only been possible thanks to the large wavelength coverage obtained by combining both PACS and SPIRE data. Indeed, with SPIRE or PACS data only, it would be not only much more difficult to show under which conditions a simple modified black-body approach does not work, but it would also be nearly impossible to quantify how model assumptions can affect the correlation of dust temperature with star formation, galaxy structure and chemical enrichment.

ACKNOWLEDGMENTS

We thank an anonymous referee for his/her very useful comments and suggestions which have significantly improved this manuscript. LC thanks B. Draine for useful discussions, and B. Catinella for comments on this manuscript. We thank all the people involved in the construction and the launch of *Herschel*.

The research leading to these results has received funding from the European Community's Seventh Framework Programme (/FP7/2007-2013/) under grant agreement No 229517, and was supported under Australian Research Council's Discovery Projects funding scheme (project number 130100664). IDL is a postdoctoral researcher of the FWO-Vlaanderen (Belgium).

PACS has been developed by a consortium of institutes led by MPE (Germany) and including UVIE (Austria); KU Leuven, CSL, IMEC (Belgium); CEA, LAM (France); MPIA (Germany); INAF-IFSI/OAA/OAP/OAT, LENS, SISSA (Italy); IAC (Spain). This development has been supported by the funding agencies BMVIT (Austria), ESA-PRODEX (Belgium), CEA/CNES (France), DLR (Germany), ASI/INAF (Italy), and CICYT/MCYT (Spain). SPIRE has been developed by a consortium of institutes led by Cardiff University (UK) and including Univ. Lethbridge (Canada); NAOC (China); CEA, LAM (France); IFSI, Univ. Padua (Italy); IAC (Spain); Stockholm Observatory (Sweden); Imperial College London, RAL, UCL-MSSL, UKATC, Univ. Sussex (UK); and Caltech, JPL, NHSC, Univ. Colorado (USA). This development has been supported by national funding agencies: CSA (Canada); NAOC (China); CEA, CNES, CNRS (France); ASI (Italy); MCINN (Spain); SNSB (Sweden); STFC (UK); and NASA (USA).

Part of the HRS data was accessed through the *Herschel* Database in Marseille (HeDaM - <http://hedam.lam.fr>) operated by CeSAM and hosted by the Laboratoire d'Astrophysique de Marseille.

We acknowledge the use of the NASA/IPAC Extragalactic Database (NED) which is operated by the Jet Propulsion Laboratory, California Institute of Technology, under contract with the National Aeronautics and Space Administration.

REFERENCES

Abazajian K. N. et al., 2009, *ApJS*, 182, 543

- Ali B., 2011, PACS Herschel, <https://nhscdmz2.ipac.caltech.edu/pacs/docs/Photometer/PICCNHSC-TMModel.pdf>
- Aniano G. et al., 2012, ApJ, 756, 138
- Auld R. et al., 2013, MNRAS, 428, 1880
- Baes M. et al., 2010, A&A, 518, L53+
- Balog Z. et al., 2013, Experimental Astronomy, in press (arXiv:1309.6099)
- Bendo G. J. et al., 2012, MNRAS, 419, 1833
- Bendo G. J., Galliano F., Madden S. C., 2012, MNRAS, 423, 197
- Bendo G. J. et al., 2013, MNRAS, 433, 3062
- Bendo G. J. et al., 2010, A&A, 518, L65+
- Bernard J.-P. et al., 2010, A&A, 518, L88
- Bianchi S., 2013, A&A, 552, A89
- Binggeli B., Sandage A., Tammann G. A., 1985, AJ, 90, 1681
- Boquien M. et al., 2011, AJ, 142, 111
- Boselli A. et al., 2010a, A&A, 518, L61+
- Boselli A. et al., 2012, A&A, 540, A54
- Boselli A., Cortese L., Boquien M., 2014, A&A in press
- Boselli A. et al., 2010b, PASP, 122, 261
- Boselli A., Gavazzi G., Sanvito G., 2003, A&A, 402, 37
- Boselli A., Hughes T. M., Cortese L., Gavazzi G., Buat V., 2013, A&A, 550, A114
- Boselli A., Sauvage M., Lequeux J., Donati A., Gavazzi G., 2003, A&A, 406, 867
- Bothwell M. S., Kennicutt R. C., Lee J. C., 2009, MNRAS, 400, 154
- Burgarella D. et al., 2013, A&A, 554, A70
- Calzetti D., Bohlin R. C., Kinney A. L., Storchi-Bergmann T., Heckman T. M., 1995, ApJ, 443, 136
- Ciesla L. et al., 2012, A&A, 543, A161
- Clemens M. S. et al., 2013, MNRAS, 433, 695
- Compiègne M. et al., 2011, A&A, 525, A103+
- Cortese L., 2012, A&A, 543, A132
- Cortese L. et al., 2012a, A&A, 544, A101
- Cortese L., Catinella B., Boissier S., Boselli A., Heinis S., 2011, MNRAS, 415, 1797
- Cortese L. et al., 2012b, A&A, 540, A52
- Cortese L., Hughes T. M., 2009, MNRAS, 400, 1225
- Dale D. A. et al., 2012, ApJ, 745, 95
- Dale D. A. et al., 2007, ApJ, 655, 863
- Davies J. I. et al., 2010, A&A, 518, L48+
- Davies J. I. et al., 2012, MNRAS, 419, 3505
- Dole H. et al., 2006, A&A, 451, 417
- Draine B. T., 2003, ARA&A, 41, 241
- Draine B. T. et al., 2013, ApJ submitted (arXiv:1306.2304)
- Draine B. T. et al., 2007, ApJ, 663, 866
- Draine B. T., Li A., 2007, ApJ, 657, 810
- Dreyer J. L. E., 1888, MmRAS, 49, 1
- Dreyer J. L. E., 1895, MmRAS, 51, 185
- Dunne L., Eales S. A., 2001, MNRAS, 327, 697
- Dunne L. et al., 2011, MNRAS, 417, 1510
- Dupac X. et al., 2003, A&A, 404, L11
- Engelbracht C. W., Rieke G. H., Gordon K. D., Smith J.-D. T., Werner M. W., Moustakas J., Willmer C. N. A., Vanzì L., 2008, ApJ, 678, 804
- Finkbeiner D. P., Davis M., Schlegel D. J., 1999, ApJ, 524, 867
- Galametz M. et al., 2012, MNRAS, 425, 763
- Galametz M. et al., 2009, A&A, 508, 645
- Galametz M. et al., 2010, A&A, 518, L55
- Galliano F. et al., 2011, A&A, 536, A88
- Galliano F., Jones A. P., Wilson C. D., Bernard J.-P., 2005, A&A, 434, 867
- Gil de Paz A., Madore B. F., 2005, ApJS, 156, 345
- Gordon K. D. et al., 2010, A&A, 518, L89+
- Griffin M. J. et al., 2010, A&A, 518, L3+
- Hao C.-N., Kennicutt R. C., Johnson B. D., Calzetti D., Dale D. A., Moustakas J., 2011, ApJ, 741, 124
- Hauser M. G., Dwek E., 2001, ARA&A, 39, 249
- Haynes M. P. et al., 2011, AJ, 142, 170
- Herschel Space Observatory 2013, SPIRE Data Reduction Guide, http://herschel.esac.esa.int/hcss-doc-11.0/print/spire_drg/spir
- Hoang T., Draine B. T., Lazarian A., 2010, ApJ, 715, 1462
- Hollenbach D., Salpeter E. E., 1971, ApJ, 163, 155
- Hughes T. M., Cortese L., Boselli A., Gavazzi G., Davies J. I., 2013, A&A, 550, A115
- James A., Dunne L., Eales S., Edmunds M. G., 2002, MNRAS, 335, 753
- James F., Roos M., 1975, Computer Physics Communications, 10, 343
- Juvela M., Montillaud J., Ysard N., Lunttila T., 2013, A&A, 556, A63
- Juvela M., Ysard N., 2012, A&A, 541, A33
- Kennicutt R. C. et al., 2011, PASP, 123, 1347
- Kewley L. J., Ellison S. L., 2008, ApJ, 681, 1183
- Magdis G. E. et al., 2011, ApJL, 740, L15
- Magnelli B. et al., 2012, A&A, 548, A22
- McKee C. F., Krumholz M. R., 2010, ApJ, 709, 308
- Meny C., Gromov V., Boudet N., Bernard J.-P., Paradis D., Nayral C., 2007, A&A, 468, 171
- Nilson P., 1973, Nova Acta Regiae Soc. Sci. Upsaliensis Ser. V, p. 0
- Ott S., 2010, in Mizumoto Y., Morita K.-I., Ohishi M., eds, Astronomical Society of the Pacific Conference Series Vol. 434, Astronomical Data Analysis Software and Systems XIX. p. 139
- Paladini R., Hendrik L., Altieri B., Ali B., 2012, PACS Herschel, <https://nhscsci.ipac.caltech.edu/pacs/docs/Photometer/PICCNHSC>
- Paradis D. et al., 2010, A&A, 520, L8+
- Pettini M., Pagel B. E. J., 2004, MNRAS, 348, L59
- Pilbratt G. L. et al., 2010, A&A, 518, L1+
- Planck Collaboration et al., 2013, A&A submitted (arXiv:1307.6815)
- Planck Collaboration et al., 2011a, A&A, 536, A1
- Planck Collaboration et al., 2011b, A&A, 536, A17
- Poglitsch A. et al., 2010, A&A, 518, L2+
- Rémy-Ruyer A. et al., 2013, A&A, 557, A95
- Roseboom I. G. et al., 2013, MNRAS
- Roussel H., 2013, PASP, 125, 1126
- Sauvage M., Thuan T. X., 1992, ApJL, 396, L69
- Schlegel D. J., Finkbeiner D. P., Davis M., 1998, ApJ, 500, 525
- Shetty R., Kauffmann J., Schnee S., Goodman A. A., 2009, ApJ, 696, 676
- Shetty R., Kauffmann J., Schnee S., Goodman A. A., Ercolano B., 2009, ApJ, 696, 2234
- Skibba R. A. et al., 2011, ApJ, 738, 89
- Skrutskie M. F. et al., 2006, AJ, 131, 1163
- Smith D. J. B. et al., 2013, MNRAS in press (arXiv:1309.4102)

- Smith M. W. L. et al., 2012, *ApJ*, 756, 40
Sodroski T. J., Dwek E., Hauser M. G., Kerr F. J., 1989, *ApJ*, 336, 762
Springob C. M., Haynes M. P., Giovanelli R., Kent B. R., 2005, *ApJS*, 160, 149
Stansberry J. A. et al., 2007, *PASP*, 119, 1038
Steinacker J., Baes M., Gordon K., 2013, *ARA&A*, 51, 63
Symeonidis M. et al., 2013, *MNRAS*, 431, 2317
Tabatabaei F. S. et al., 2013, *A&A* in press (arXiv:1310.4155)
Vlahakis C., Dunne L., Eales S., 2005, *MNRAS*, 364, 1253
Walterbos R. A. M., Greenawalt B., 1996, *ApJ*, 460, 696
Werner M. W. et al., 2004, *ApJS*, 154, 1
Zwicky F., Herzog E., Wild P., 1961, *Catalogue of galaxies and of clusters of galaxies*. Pasadena: California Institute of Technology (CIT)

Table 1 – Continued.

HRS	CGCG	VCC	UGC	NGC	IC	R.A. (J.2000) hh:mm:ss.ss	Dec (J.2000) dd:mm:ss.s	Type	Flag100	F ₁₀₀ Jy	σ_{100} Jy	Flag160	F ₁₆₀ Jy	σ_{160} Jy	a arcsec	b arcsec	P.A. degree	Proposal ID
312	47-020	0	9183	5576	0	14:21:03.68	+03:16:15.6	0	0	0.236	0.0	0	0.187	0.0	31.	31.	0.	OT1_lcortese_1
313	47-022	0	9187	5577	0	14:21:13.11	+03:26:08.8	6	1	2.55	0.802	1	3.803	0.819	154.	65.	55.	OT1_lcortese_1
314	19-012	0	9215	0	0	14:23:27.12	+01:43:34.7	9	1	2.772	0.417	1	3.316	0.23	95.	63.	-15.	OT1_lcortese_1
315	220-015	0	9242	0	0	14:25:21.02	+39:32:22.5	7	1	1.056	0.409	1	0.863	0.327	176.	29.	71.	OT1_lcortese_1
316	47-063	0	9308	5638	0	14:29:40.39	+03:14:00.2	0	0	0.15	0.0	0	0.169	0.0	24.	24.	0.	OT1_lcortese_1
317	47-066	0	9311	0	1022	14:30:01.85	+03:46:22.3	5	1	0.222	0.1	1	0.475	0.062	34.	28.	-15.	OT1_lcortese_1
318	47-070	0	9328	5645	0	14:30:39.35	+07:16:30.3	9	1	4.998	0.406	1	6.331	0.483	101.	63.	-75.	OT1_lcortese_1
319	75-064	0	9353	5669	0	14:32:43.88	+09:53:30.5	8	1	6.923	0.996	1	8.145	1.192	167.	118.	61.	OT1_lcortese_1
320	47-090	0	9363	5668	0	14:33:24.34	+04:27:01.6	9	1	7.735	2.205	1	10.256	1.478	152.	145.	17.	OT1_lcortese_1
321	47-123	0	9427	5692	0	14:38:18.12	+03:24:37.2	5	1	2.942	0.17	1	3.164	0.179	50.	33.	40.	OT1_lcortese_1
322	47-127	0	9436	5701	0	14:39:11.06	+05:21:48.8	3	1	1.453	1.035	1	1.859	1.201	124.	120.	-90.	OT1_lcortese_1
323	48-004	0	9483	0	1048	14:42:57.88	+04:53:24.5	5	1	5.689	0.391	1	7.547	0.575	101.	47.	-17.	OT1_lcortese_1

Table 3: Best-fitting dust temperatures and masses for a single modified black-body with $\beta=2$ and β =free. Only galaxies for which the reduced χ^2 corresponds to a probability $P \geq 95\%$ are shown.

HRS	D Mpc	$\beta=2$		β	β =free	
		T K	$\log(M_{dust})$ M_{\odot}		T K	$\log(M_{dust})$ M_{\odot}
1	16.79	21.7 ^{+1.0} _{-1.0}	5.93 ^{+0.07} _{-0.07}	2.0 ^{+0.5} _{-0.5}	21.5 ^{+3.8} _{-3.1}	5.94 ^{+0.15} _{-0.14}
2	18.44	24.0 ^{+0.6} _{-0.6}	6.27 ^{+0.04} _{-0.04}	2.3 ^{+0.3} _{-0.3}	21.6 ^{+1.9} _{-1.6}	6.36 ^{+0.07} _{-0.07}
5	16.71	22.4 ^{+0.4} _{-0.4}	6.62 ^{+0.02} _{-0.02}	2.2 ^{+0.2} _{-0.2}	20.9 ^{+1.0} _{-1.0}	6.68 ^{+0.05} _{-0.04}
6	18.89	13.9 ^{+0.8} _{-0.8}	6.80 ^{+0.11} _{-0.11}	1.4 ^{+1.0} _{-0.8}	16.6 ^{+5.8} _{-4.0}	6.57 ^{+0.37} _{-0.33}
7	18.77	25.7 ^{+0.3} _{-0.3}	6.26 ^{+0.01} _{-0.01}	2.2 ^{+0.1} _{-0.1}	23.9 ^{+0.8} _{-0.8}	6.31 ^{+0.03} _{-0.03}
8	19.37	15.3 ^{+0.8} _{-0.7}	7.48 ^{+0.06} _{-0.06}	1.3 ^{+0.4} _{-0.3}	20.9 ^{+3.6} _{-3.2}	7.11 ^{+0.18} _{-0.16}
9	20.21	21.8 ^{+0.9} _{-0.9}	6.53 ^{+0.06} _{-0.05}	2.5 ^{+0.4} _{-0.4}	18.9 ^{+2.1} _{-2.0}	6.66 ^{+0.12} _{-0.12}
11	18.93	-	-	1.6 ^{+0.1} _{-0.1}	23.7 ^{+1.0} _{-1.0}	6.82 ^{+0.04} _{-0.04}
12	19.89	23.6 ^{+0.7} _{-0.7}	5.72 ^{+0.05} _{-0.05}	1.2 ^{+0.4} _{-0.3}	31.9 ^{+6.0} _{-4.3}	5.51 ^{+0.11} _{-0.12}
13	22.47	21.8 ^{+0.3} _{-0.3}	7.57 ^{+0.02} _{-0.02}	1.9 ^{+0.1} _{-0.1}	22.5 ^{+0.7} _{-0.7}	7.54 ^{+0.03} _{-0.03}
15	18.57	19.2 ^{+0.7} _{-0.7}	7.60 ^{+0.06} _{-0.05}	1.7 ^{+0.3} _{-0.3}	20.8 ^{+2.7} _{-2.3}	7.52 ^{+0.12} _{-0.12}
16	18.00	19.7 ^{+0.4} _{-0.4}	7.17 ^{+0.03} _{-0.03}	1.9 ^{+0.2} _{-0.2}	20.0 ^{+1.2} _{-1.2}	7.16 ^{+0.06} _{-0.06}
17	18.30	21.2 ^{+0.4} _{-0.4}	7.17 ^{+0.03} _{-0.03}	1.7 ^{+0.1} _{-0.1}	23.6 ^{+1.4} _{-1.3}	7.08 ^{+0.05} _{-0.05}
18	22.91	20.7 ^{+0.7} _{-0.7}	6.61 ^{+0.05} _{-0.05}	1.9 ^{+0.3} _{-0.3}	21.3 ^{+2.3} _{-2.0}	6.59 ^{+0.10} _{-0.09}
19	23.29	21.0 ^{+0.6} _{-0.6}	6.99 ^{+0.04} _{-0.04}	1.5 ^{+0.2} _{-0.2}	25.3 ^{+2.7} _{-2.3}	6.83 ^{+0.09} _{-0.09}
21	16.89	-	-	0.8 ^{+0.5} _{-0.4}	29.3 ^{+8.8} _{-5.7}	5.85 ^{+0.19} _{-0.20}
22	20.20	20.4 ^{+0.9} _{-0.8}	6.15 ^{+0.10} _{-0.10}	1.2 ^{+0.6} _{-0.6}	26.1 ^{+7.4} _{-4.6}	5.96 ^{+0.18} _{-0.21}
23	21.44	23.3 ^{+0.3} _{-0.3}	7.31 ^{+0.02} _{-0.02}	1.9 ^{+0.1} _{-0.1}	24.1 ^{+0.8} _{-0.8}	7.28 ^{+0.03} _{-0.03}
24	22.64	20.5 ^{+0.5} _{-0.5}	7.50 ^{+0.03} _{-0.03}	1.8 ^{+0.2} _{-0.2}	21.8 ^{+1.4} _{-1.3}	7.44 ^{+0.06} _{-0.06}
26	22.41	-	-	0.9 ^{+0.3} _{-0.3}	29.2 ^{+4.9} _{-3.7}	6.01 ^{+0.11} _{-0.12}
27	24.77	24.5 ^{+0.6} _{-0.6}	6.56 ^{+0.03} _{-0.03}	2.2 ^{+0.2} _{-0.2}	23.3 ^{+1.9} _{-1.7}	6.60 ^{+0.07} _{-0.07}
28	19.03	21.4 ^{+0.3} _{-0.3}	6.76 ^{+0.02} _{-0.02}	-	-	-
29	15.73	20.2 ^{+0.6} _{-0.6}	6.56 ^{+0.05} _{-0.05}	1.6 ^{+0.3} _{-0.3}	23.2 ^{+2.7} _{-2.3}	6.44 ^{+0.10} _{-0.10}
30	15.79	19.5 ^{+0.7} _{-0.7}	6.71 ^{+0.06} _{-0.06}	1.4 ^{+0.3} _{-0.3}	24.2 ^{+3.6} _{-2.9}	6.51 ^{+0.12} _{-0.12}
31	19.63	23.1 ^{+0.7} _{-0.7}	7.06 ^{+0.04} _{-0.04}	1.3 ^{+0.3} _{-0.3}	29.4 ^{+4.1} _{-3.2}	6.87 ^{+0.10} _{-0.10}
33	20.46	21.3 ^{+0.4} _{-0.4}	6.98 ^{+0.03} _{-0.03}	1.8 ^{+0.2} _{-0.2}	22.7 ^{+1.4} _{-1.3}	6.93 ^{+0.05} _{-0.05}
34	16.14	19.1 ^{+0.5} _{-0.5}	7.07 ^{+0.04} _{-0.04}	1.6 ^{+0.2} _{-0.2}	21.8 ^{+1.6} _{-1.5}	6.95 ^{+0.07} _{-0.07}
36	21.94	26.3 ^{+0.4} _{-0.4}	7.33 ^{+0.02} _{-0.02}	2.0 ^{+0.1} _{-0.1}	26.3 ^{+1.2} _{-1.1}	7.33 ^{+0.04} _{-0.04}
37	19.61	22.6 ^{+0.4} _{-0.4}	6.73 ^{+0.03} _{-0.03}	2.0 ^{+0.2} _{-0.2}	22.5 ^{+1.5} _{-1.3}	6.73 ^{+0.06} _{-0.06}
38	20.27	-	-	1.2 ^{+0.2} _{-0.2}	26.2 ^{+3.2} _{-2.7}	6.41 ^{+0.10} _{-0.10}
39	22.24	18.3 ^{+1.0} _{-1.1}	6.65 ^{+0.08} _{-0.07}	1.1 ^{+0.4} _{-0.4}	24.7 ^{+4.4} _{-3.5}	6.37 ^{+0.14} _{-0.14}
40	22.63	23.7 ^{+0.4} _{-0.4}	6.71 ^{+0.02} _{-0.02}	1.8 ^{+0.2} _{-0.2}	25.5 ^{+1.7} _{-1.5}	6.65 ^{+0.05} _{-0.05}
41	18.61	18.8 ^{+0.7} _{-0.7}	6.56 ^{+0.05} _{-0.05}	1.4 ^{+0.3} _{-0.3}	23.9 ^{+3.2} _{-2.7}	6.33 ^{+0.12} _{-0.11}
42	17.04	20.5 ^{+0.7} _{-0.7}	7.32 ^{+0.05} _{-0.05}	1.7 ^{+0.3} _{-0.3}	22.7 ^{+2.4} _{-2.1}	7.22 ^{+0.10} _{-0.10}
44	16.01	23.3 ^{+0.6} _{-0.6}	6.17 ^{+0.04} _{-0.04}	1.3 ^{+0.3} _{-0.2}	30.1 ^{+3.8} _{-3.0}	5.97 ^{+0.08} _{-0.09}
46	21.34	24.5 ^{+0.4} _{-0.4}	6.62 ^{+0.02} _{-0.02}	2.1 ^{+0.2} _{-0.2}	24.0 ^{+1.4} _{-1.2}	6.64 ^{+0.05} _{-0.05}
47	21.53	20.2 ^{+0.9} _{-0.9}	6.83 ^{+0.06} _{-0.06}	1.3 ^{+0.3} _{-0.3}	25.3 ^{+4.0} _{-3.1}	6.63 ^{+0.12} _{-0.13}
48	16.50	21.5 ^{+0.5} _{-0.5}	7.53 ^{+0.04} _{-0.04}	1.9 ^{+0.3} _{-0.3}	22.0 ^{+1.9} _{-1.7}	7.51 ^{+0.07} _{-0.07}
50	21.43	-	-	2.2 ^{+0.1} _{-0.1}	22.9 ^{+0.7} _{-0.7}	7.31 ^{+0.03} _{-0.03}
51	18.56	-	-	1.4 ^{+0.2} _{-0.2}	26.0 ^{+2.1} _{-1.8}	6.65 ^{+0.07} _{-0.07}
52	17.20	20.9 ^{+1.3} _{-1.4}	6.11 ^{+0.09} _{-0.09}	1.8 ^{+0.5} _{-0.5}	22.1 ^{+4.6} _{-3.6}	6.05 ^{+0.17} _{-0.17}
53	15.14	-	-	1.5 ^{+0.1} _{-0.1}	24.3 ^{+1.5} _{-1.4}	6.86 ^{+0.06} _{-0.06}
54	17.77	20.1 ^{+0.9} _{-0.9}	6.71 ^{+0.06} _{-0.05}	1.8 ^{+0.3} _{-0.3}	21.9 ^{+3.0} _{-2.6}	6.63 ^{+0.13} _{-0.12}
55	16.54	20.9 ^{+0.4} _{-0.4}	7.05 ^{+0.03} _{-0.03}	1.9 ^{+0.2} _{-0.2}	21.4 ^{+1.3} _{-1.2}	7.02 ^{+0.06} _{-0.06}
57	16.51	20.9 ^{+0.3} _{-0.3}	7.25 ^{+0.02} _{-0.02}	2.1 ^{+0.1} _{-0.1}	20.4 ^{+1.0} _{-0.9}	7.28 ^{+0.05} _{-0.05}
59	24.53	19.6 ^{+0.4} _{-0.4}	7.24 ^{+0.04} _{-0.04}	1.6 ^{+0.2} _{-0.2}	22.2 ^{+1.8} _{-1.6}	7.12 ^{+0.07} _{-0.07}
60	15.14	21.3 ^{+0.4} _{-0.4}	6.92 ^{+0.03} _{-0.03}	2.0 ^{+0.1} _{-0.1}	21.1 ^{+1.2} _{-1.1}	6.92 ^{+0.06} _{-0.06}
61	17.39	19.3 ^{+0.8} _{-0.8}	6.21 ^{+0.06} _{-0.06}	1.3 ^{+0.4} _{-0.3}	24.0 ^{+3.6} _{-2.9}	6.02 ^{+0.12} _{-0.12}
62	22.44	-	-	1.0 ^{+0.3} _{-0.3}	26.8 ^{+3.9} _{-3.1}	6.73 ^{+0.11} _{-0.11}
63	18.41	18.7 ^{+0.5} _{-0.5}	7.39 ^{+0.04} _{-0.04}	1.8 ^{+0.2} _{-0.2}	20.1 ^{+1.6} _{-1.5}	7.31 ^{+0.08} _{-0.08}
64	17.33	17.7 ^{+0.9} _{-0.9}	6.65 ^{+0.08} _{-0.07}	1.3 ^{+0.4} _{-0.3}	23.4 ^{+4.0} _{-3.3}	6.36 ^{+0.15} _{-0.15}
65	19.76	18.5 ^{+1.2} _{-1.2}	6.77 ^{+0.09} _{-0.08}	1.0 ^{+0.4} _{-0.4}	27.6 ^{+6.4} _{-4.6}	6.40 ^{+0.17} _{-0.17}
66	20.97	23.9 ^{+0.2} _{-0.2}	7.33 ^{+0.01} _{-0.01}	-	-	-
67	20.51	17.9 ^{+0.9} _{-0.9}	6.65 ^{+0.08} _{-0.08}	1.2 ^{+0.4} _{-0.4}	23.2 ^{+4.1} _{-3.2}	6.40 ^{+0.15} _{-0.15}
69	16.73	18.0 ^{+1.2} _{-1.2}	7.04 ^{+0.10} _{-0.09}	1.5 ^{+0.5} _{-0.5}	21.5 ^{+5.1} _{-3.8}	6.85 ^{+0.22} _{-0.21}

Continued on the next page. . .

Table 3 – Continued.

HRS	D Mpc	$\beta=2$			$\beta=\text{free}$		
		T K	$\log(M_{\text{dust}})$ M_{\odot}	β	T K	$\log(M_{\text{dust}})$ M_{\odot}	
70	23.10	20.7 ^{+0.6} _{-0.6}	6.64 ^{+0.04} _{-0.04}	1.7 ^{+0.2} _{-0.2}	23.0 ^{+2.0} _{-1.8}	6.55 ^{+0.08} _{-0.08}	
72	22.53	24.7 ^{+1.0} _{-0.9}	6.31 ^{+0.06} _{-0.06}	1.5 ^{+0.5} _{-0.5}	29.5 ^{+7.5} _{-5.0}	6.19 ^{+0.14} _{-0.16}	
73	15.00	19.3 ^{+0.3} _{-0.3}	7.77 ^{+0.03} _{-0.03}	2.2 ^{+0.2} _{-0.2}	18.3 ^{+1.1} _{-1.0}	7.83 ^{+0.07} _{-0.07}	
74	15.83	23.9 ^{+0.4} _{-0.4}	6.95 ^{+0.03} _{-0.03}	2.0 ^{+0.2} _{-0.2}	24.1 ^{+1.6} _{-1.4}	6.94 ^{+0.05} _{-0.05}	
75	18.33	15.6 ^{+0.9} _{-0.9}	6.34 ^{+0.11} _{-0.10}	1.6 ^{+0.7} _{-0.6}	17.4 ^{+4.0} _{-3.2}	6.21 ^{+0.25} _{-0.22}	
76	15.27	18.8 ^{+1.0} _{-1.0}	6.19 ^{+0.08} _{-0.08}	1.1 ^{+0.4} _{-0.4}	26.2 ^{+5.0} _{-3.8}	5.89 ^{+0.14} _{-0.15}	
77	20.83	22.4 ^{+0.3} _{-0.3}	7.93 ^{+0.01} _{-0.01}	2.2 ^{+0.1} _{-0.1}	21.3 ^{+0.7} _{-0.7}	7.98 ^{+0.03} _{-0.03}	
78	18.13	19.8 ^{+0.5} _{-0.5}	6.67 ^{+0.05} _{-0.05}	1.4 ^{+0.4} _{-0.4}	24.0 ^{+2.7} _{-2.7}	6.49 ^{+0.12} _{-0.13}	
79	21.54	19.9 ^{+1.0} _{-1.0}	6.49 ^{+0.08} _{-0.08}	1.4 ^{+0.6} _{-0.6}	23.9 ^{+6.2} _{-4.1}	6.33 ^{+0.18} _{-0.20}	
80	17.00	17.7 ^{+1.1} _{-1.1}	6.84 ^{+0.09} _{-0.09}	1.7 ^{+0.6} _{-0.6}	19.3 ^{+4.2} _{-3.3}	6.75 ^{+0.21} _{-0.20}	
81	17.00	22.4 ^{+0.3} _{-0.3}	7.14 ^{+0.02} _{-0.02}	2.0 ^{+0.1} _{-0.1}	22.8 ^{+1.0} _{-0.9}	7.12 ^{+0.04} _{-0.04}	
82	17.00	23.4 ^{+1.0} _{-1.0}	6.09 ^{+0.06} _{-0.06}	1.7 ^{+0.4} _{-0.4}	25.7 ^{+4.3} _{-3.4}	6.02 ^{+0.12} _{-0.13}	
83	17.60	19.8 ^{+1.3} _{-1.4}	6.00 ^{+0.10} _{-0.10}	0.9 ^{+0.4} _{-0.4}	30.4 ^{+8.6} _{-5.7}	5.65 ^{+0.18} _{-0.18}	
84	17.00	21.2 ^{+0.4} _{-0.4}	6.40 ^{+0.03} _{-0.03}	2.0 ^{+0.2} _{-0.2}	21.0 ^{+1.3} _{-1.2}	6.40 ^{+0.06} _{-0.06}	
85	15.31	21.4 ^{+0.4} _{-0.4}	7.36 ^{+0.03} _{-0.03}	1.8 ^{+0.1} _{-0.1}	23.2 ^{+1.3} _{-1.2}	7.29 ^{+0.05} _{-0.05}	
86	17.00	-	-	1.2 ^{+0.2} _{-0.2}	26.2 ^{+3.4} _{-2.9}	6.86 ^{+0.11} _{-0.11}	
87	17.00	22.8 ^{+1.1} _{-1.0}	6.15 ^{+0.07} _{-0.07}	2.0 ^{+0.5} _{-0.5}	22.5 ^{+4.3} _{-3.2}	6.16 ^{+0.15} _{-0.15}	
88	17.00	20.5 ^{+0.9} _{-0.9}	7.26 ^{+0.06} _{-0.05}	1.3 ^{+0.3} _{-0.3}	26.3 ^{+3.8} _{-3.0}	7.03 ^{+0.11} _{-0.11}	
89	17.00	-	-	1.1 ^{+0.1} _{-0.1}	24.9 ^{+1.5} _{-1.4}	7.19 ^{+0.06} _{-0.05}	
91	17.00	19.6 ^{+0.3} _{-0.3}	7.81 ^{+0.03} _{-0.03}	2.0 ^{+0.2} _{-0.2}	19.8 ^{+1.2} _{-1.1}	7.80 ^{+0.06} _{-0.06}	
92	17.00	19.4 ^{+0.6} _{-0.6}	6.59 ^{+0.05} _{-0.05}	1.6 ^{+0.3} _{-0.3}	22.1 ^{+2.4} _{-2.0}	6.46 ^{+0.10} _{-0.10}	
93	15.59	21.0 ^{+0.8} _{-0.8}	6.40 ^{+0.07} _{-0.07}	2.0 ^{+0.5} _{-0.5}	20.9 ^{+3.6} _{-2.8}	6.40 ^{+0.14} _{-0.15}	
94	17.00	-	-	1.0 ^{+0.2} _{-0.2}	23.5 ^{+1.9} _{-1.7}	6.87 ^{+0.07} _{-0.07}	
95	17.00	24.5 ^{+0.3} _{-0.3}	6.64 ^{+0.02} _{-0.02}	2.2 ^{+0.1} _{-0.1}	22.9 ^{+0.9} _{-0.9}	6.69 ^{+0.04} _{-0.04}	
96	17.00	22.3 ^{+0.3} _{-0.3}	7.31 ^{+0.02} _{-0.02}	2.1 ^{+0.1} _{-0.1}	21.3 ^{+0.8} _{-0.8}	7.35 ^{+0.04} _{-0.04}	
97	17.00	18.7 ^{+0.3} _{-0.3}	7.77 ^{+0.02} _{-0.02}	1.9 ^{+0.1} _{-0.1}	19.1 ^{+0.8} _{-0.8}	7.75 ^{+0.04} _{-0.04}	
98	17.00	-	-	1.4 ^{+0.2} _{-0.2}	22.7 ^{+1.5} _{-1.3}	6.80 ^{+0.06} _{-0.06}	
99	17.00	22.5 ^{+0.4} _{-0.4}	6.00 ^{+0.03} _{-0.03}	2.4 ^{+0.2} _{-0.2}	20.2 ^{+1.2} _{-1.2}	6.09 ^{+0.06} _{-0.06}	
100	17.00	-	-	2.3 ^{+0.1} _{-0.1}	19.8 ^{+0.5} _{-0.5}	7.17 ^{+0.03} _{-0.03}	
102	17.00	-	-	2.3 ^{+0.1} _{-0.1}	21.0 ^{+1.0} _{-0.9}	8.06 ^{+0.04} _{-0.05}	
106	23.00	20.5 ^{+1.2} _{-1.2}	6.74 ^{+0.08} _{-0.08}	1.7 ^{+0.5} _{-0.5}	22.8 ^{+4.7} _{-3.6}	6.65 ^{+0.17} _{-0.17}	
107	17.00	19.2 ^{+0.6} _{-0.6}	6.40 ^{+0.05} _{-0.05}	1.6 ^{+0.3} _{-0.3}	21.8 ^{+2.6} _{-2.2}	6.29 ^{+0.10} _{-0.10}	
108	23.00	22.6 ^{+0.9} _{-0.9}	6.24 ^{+0.06} _{-0.06}	2.2 ^{+0.5} _{-0.4}	21.4 ^{+3.1} _{-2.5}	6.29 ^{+0.12} _{-0.11}	
109	17.00	-	-	1.2 ^{+0.2} _{-0.2}	24.5 ^{+2.2} _{-1.9}	6.56 ^{+0.08} _{-0.08}	
110	17.00	-	-	1.4 ^{+0.2} _{-0.2}	25.4 ^{+1.9} _{-1.7}	6.76 ^{+0.06} _{-0.06}	
111	17.00	-	-	2.3 ^{+0.1} _{-0.1}	19.3 ^{+0.5} _{-0.4}	7.43 ^{+0.02} _{-0.02}	
112	23.00	21.4 ^{+0.8} _{-0.8}	6.34 ^{+0.06} _{-0.06}	1.6 ^{+0.4} _{-0.4}	24.2 ^{+3.7} _{-2.9}	6.23 ^{+0.12} _{-0.12}	
113	17.00	19.7 ^{+0.2} _{-0.2}	7.63 ^{+0.01} _{-0.01}	2.2 ^{+0.1} _{-0.1}	18.7 ^{+2.9} _{-2.0}	7.69 ^{+0.03} _{-0.03}	
114	17.00	22.9 ^{+0.3} _{-0.3}	7.91 ^{+0.02} _{-0.02}	2.0 ^{+0.1} _{-0.1}	23.2 ^{+1.0} _{-0.9}	7.91 ^{+0.04} _{-0.04}	
115	17.00	21.6 ^{+0.6} _{-0.6}	6.04 ^{+0.04} _{-0.05}	1.8 ^{+0.3} _{-0.3}	23.1 ^{+2.5} _{-2.1}	5.99 ^{+0.09} _{-0.09}	
117	23.00	20.2 ^{+0.4} _{-0.4}	7.24 ^{+0.03} _{-0.03}	2.3 ^{+0.2} _{-0.2}	18.7 ^{+1.1} _{-1.0}	7.31 ^{+0.06} _{-0.06}	
118	17.00	20.4 ^{+1.1} _{-1.1}	6.32 ^{+0.08} _{-0.08}	1.2 ^{+0.5} _{-0.4}	26.7 ^{+6.2} _{-4.3}	6.09 ^{+0.16} _{-0.17}	
119	17.00	22.3 ^{+0.5} _{-0.5}	6.82 ^{+0.04} _{-0.04}	2.6 ^{+0.3} _{-0.3}	19.2 ^{+1.6} _{-1.4}	6.95 ^{+0.08} _{-0.08}	
120	17.00	20.3 ^{+0.4} _{-0.4}	6.92 ^{+0.04} _{-0.04}	2.4 ^{+0.3} _{-0.3}	18.4 ^{+1.4} _{-1.3}	7.01 ^{+0.07} _{-0.07}	
121	23.00	20.4 ^{+0.2} _{-0.2}	7.25 ^{+0.02} _{-0.02}	2.1 ^{+0.1} _{-0.1}	20.1 ^{+0.7} _{-0.6}	7.27 ^{+0.03} _{-0.03}	
122	17.00	21.1 ^{+0.3} _{-0.3}	8.09 ^{+0.03} _{-0.03}	2.2 ^{+0.2} _{-0.2}	19.9 ^{+1.1} _{-1.1}	8.15 ^{+0.05} _{-0.05}	
123	17.00	19.0 ^{+0.7} _{-0.7}	6.67 ^{+0.05} _{-0.05}	2.0 ^{+0.3} _{-0.3}	19.2 ^{+2.1} _{-1.9}	6.66 ^{+0.12} _{-0.11}	
124	17.00	18.9 ^{+0.7} _{-0.7}	6.98 ^{+0.05} _{-0.05}	1.8 ^{+0.4} _{-0.3}	19.9 ^{+2.4} _{-2.0}	6.93 ^{+0.12} _{-0.11}	
127	23.00	20.4 ^{+0.3} _{-0.3}	7.14 ^{+0.02} _{-0.02}	2.0 ^{+0.1} _{-0.1}	20.6 ^{+0.9} _{-0.8}	7.13 ^{+0.04} _{-0.04}	
128	23.00	17.7 ^{+0.5} _{-0.5}	6.76 ^{+0.04} _{-0.04}	2.0 ^{+0.3} _{-0.3}	17.8 ^{+1.7} _{-1.5}	6.76 ^{+0.10} _{-0.10}	
130	17.00	20.5 ^{+0.7} _{-0.7}	6.52 ^{+0.05} _{-0.05}	1.7 ^{+0.3} _{-0.3}	22.6 ^{+2.7} _{-2.3}	6.44 ^{+0.10} _{-0.10}	
131	23.00	19.1 ^{+0.8} _{-0.8}	6.55 ^{+0.07} _{-0.07}	2.5 ^{+0.6} _{-0.5}	16.7 ^{+2.7} _{-2.3}	6.69 ^{+0.17} _{-0.16}	
132	23.00	-	-	0.8 ^{+0.4} _{-0.4}	33.8 ^{+5.8} _{-5.8}	6.12 ^{+0.15} _{-0.17}	
133	17.90	-	-	0.6 ^{+0.3} _{-0.3}	27.1 ^{+4.9} _{-4.0}	6.53 ^{+0.15} _{-0.14}	
134	23.00	20.8 ^{+0.7} _{-0.7}	6.70 ^{+0.05} _{-0.05}	2.3 ^{+0.4} _{-0.4}	19.1 ^{+2.2} _{-1.9}	6.77 ^{+0.11} _{-0.11}	
136	23.00	22.4 ^{+0.3} _{-0.3}	6.75 ^{+0.02} _{-0.02}	2.4 ^{+0.2} _{-0.2}	20.0 ^{+1.0} _{-0.9}	6.84 ^{+0.05} _{-0.05}	
139	23.00	21.3 ^{+0.6} _{-0.6}	6.59 ^{+0.04} _{-0.04}	1.4 ^{+0.3} _{-0.3}	26.1 ^{+3.4} _{-2.7}	6.42 ^{+0.10} _{-0.10}	

Continued on the next page...

Table 3 – Continued.

HRS	D Mpc	$\beta=2$			$\beta=\text{free}$		
		T K	$\log(M_{\text{dust}})$ M_{\odot}	β	T K	$\log(M_{\text{dust}})$ M_{\odot}	
140	17.00	$17.4^{+0.8}_{-0.8}$	$7.01^{+0.08}_{-0.07}$	$2.1^{+0.5}_{-0.4}$	$17.1^{+2.5}_{-2.2}$	$7.03^{+0.17}_{-0.15}$	
141	23.00	$18.6^{+0.3}_{-0.3}$	$7.39^{+0.03}_{-0.03}$	$2.3^{+0.3}_{-0.2}$	$17.4^{+1.1}_{-1.0}$	$7.45^{+0.07}_{-0.06}$	
143	23.00	-	-	$1.5^{+0.1}_{-0.1}$	$23.3^{+1.2}_{-1.1}$	$7.17^{+0.05}_{-0.05}$	
144	17.00	$23.9^{+0.3}_{-0.3}$	$7.07^{+0.02}_{-0.02}$	$1.9^{+0.2}_{-0.2}$	$24.4^{+1.5}_{-1.3}$	$7.05^{+0.05}_{-0.05}$	
146	23.00	$20.1^{+0.4}_{-0.4}$	$6.87^{+0.03}_{-0.03}$	$1.5^{+0.2}_{-0.2}$	$24.1^{+1.9}_{-1.7}$	$6.71^{+0.07}_{-0.07}$	
147	17.00	$17.9^{+0.5}_{-0.5}$	$6.92^{+0.04}_{-0.04}$	$1.6^{+0.2}_{-0.2}$	$21.0^{+1.6}_{-1.5}$	$6.76^{+0.08}_{-0.07}$	
148	17.00	-	-	$1.2^{+0.2}_{-0.2}$	$24.1^{+1.9}_{-1.7}$	$6.82^{+0.07}_{-0.07}$	
149	17.00	-	-	$2.2^{+0.1}_{-0.1}$	$19.9^{+0.5}_{-0.5}$	$7.47^{+0.03}_{-0.02}$	
151	17.00	$21.1^{+0.7}_{-0.7}$	$6.68^{+0.05}_{-0.05}$	$1.7^{+0.3}_{-0.3}$	$23.3^{+3.1}_{-2.5}$	$6.60^{+0.11}_{-0.11}$	
152	17.00	$24.4^{+0.4}_{-0.4}$	$6.54^{+0.02}_{-0.02}$	$2.3^{+0.2}_{-0.2}$	$22.4^{+1.4}_{-1.3}$	$6.61^{+0.05}_{-0.05}$	
153	17.00	$20.6^{+0.5}_{-0.5}$	$6.72^{+0.04}_{-0.04}$	$1.9^{+0.3}_{-0.2}$	$21.2^{+1.8}_{-1.6}$	$6.69^{+0.08}_{-0.08}$	
154	23.00	$17.9^{+0.8}_{-0.9}$	$7.13^{+0.08}_{-0.07}$	$1.0^{+0.4}_{-0.4}$	$24.5^{+4.4}_{-3.4}$	$6.84^{+0.14}_{-0.15}$	
156	17.00	$23.9^{+0.4}_{-0.4}$	$7.05^{+0.02}_{-0.02}$	$2.2^{+0.1}_{-0.1}$	$22.6^{+1.7}_{-0.9}$	$7.10^{+0.04}_{-0.04}$	
158	23.00	$17.7^{+0.8}_{-0.9}$	$6.86^{+0.08}_{-0.08}$	$0.9^{+0.5}_{-0.4}$	$24.4^{+4.9}_{-3.6}$	$6.56^{+0.15}_{-0.16}$	
159	23.00	$25.2^{+0.5}_{-0.5}$	$6.75^{+0.03}_{-0.03}$	$2.2^{+0.3}_{-0.3}$	$23.6^{+2.0}_{-1.8}$	$6.80^{+0.06}_{-0.06}$	
160	23.00	$19.8^{+0.5}_{-0.5}$	$7.24^{+0.03}_{-0.03}$	$2.1^{+0.2}_{-0.2}$	$19.4^{+1.4}_{-1.3}$	$7.26^{+0.07}_{-0.07}$	
162	17.00	$25.1^{+0.8}_{-0.7}$	$6.35^{+0.06}_{-0.06}$	$2.7^{+0.4}_{-0.4}$	$20.9^{+2.3}_{-2.0}$	$6.48^{+0.09}_{-0.09}$	
163	17.00	$21.3^{+0.4}_{-0.4}$	$7.19^{+0.03}_{-0.04}$	$2.1^{+0.3}_{-0.2}$	$20.8^{+1.7}_{-1.5}$	$7.21^{+0.08}_{-0.08}$	
165	23.00	$20.4^{+1.0}_{-1.0}$	$6.44^{+0.07}_{-0.07}$	$1.6^{+0.4}_{-0.4}$	$23.5^{+3.8}_{-3.1}$	$6.32^{+0.13}_{-0.13}$	
167	23.00	$19.6^{+0.4}_{-0.4}$	$6.76^{+0.04}_{-0.04}$	$2.7^{+0.3}_{-0.3}$	$16.5^{+1.2}_{-1.1}$	$6.93^{+0.08}_{-0.08}$	
168	23.00	$21.0^{+0.6}_{-0.6}$	$6.35^{+0.05}_{-0.05}$	$1.2^{+0.3}_{-0.3}$	$27.0^{+4.0}_{-3.1}$	$6.15^{+0.11}_{-0.11}$	
169	24.30	$20.1^{+0.7}_{-0.7}$	$6.73^{+0.05}_{-0.05}$	$1.8^{+0.3}_{-0.3}$	$21.4^{+2.4}_{-2.0}$	$6.68^{+0.10}_{-0.10}$	
170	17.00	$19.9^{+1.1}_{-1.2}$	$7.29^{+0.08}_{-0.08}$	$1.9^{+0.5}_{-0.5}$	$20.8^{+4.4}_{-3.3}$	$7.25^{+0.20}_{-0.20}$	
171	23.00	$23.5^{+0.4}_{-0.4}$	$6.76^{+0.02}_{-0.02}$	$2.2^{+0.2}_{-0.2}$	$22.0^{+1.3}_{-1.2}$	$6.81^{+0.05}_{-0.05}$	
172	17.00	$22.2^{+0.7}_{-0.7}$	$6.63^{+0.04}_{-0.04}$	$2.3^{+0.3}_{-0.3}$	$20.1^{+2.0}_{-1.7}$	$6.72^{+0.10}_{-0.09}$	
173	17.00	$23.9^{+0.4}_{-0.4}$	$6.82^{+0.02}_{-0.02}$	$2.2^{+0.2}_{-0.2}$	$22.3^{+1.4}_{-1.3}$	$6.88^{+0.06}_{-0.06}$	
174	17.00	$25.9^{+0.3}_{-0.3}$	$6.23^{+0.01}_{-0.01}$	-	-	-	
176	23.00	$21.9^{+0.4}_{-0.4}$	$6.81^{+0.03}_{-0.03}$	$2.3^{+0.2}_{-0.2}$	$20.0^{+1.2}_{-1.1}$	$6.90^{+0.06}_{-0.06}$	
177	17.00	$22.8^{+0.3}_{-0.3}$	$6.57^{+0.02}_{-0.02}$	$1.9^{+0.2}_{-0.2}$	$23.4^{+1.3}_{-1.1}$	$6.55^{+0.05}_{-0.05}$	
180	17.00	$25.6^{+0.9}_{-0.9}$	$5.72^{+0.06}_{-0.07}$	$3.5^{+0.8}_{-0.7}$	$17.9^{+3.2}_{-2.5}$	$5.96^{+0.12}_{-0.13}$	
182	17.00	$20.6^{+0.3}_{-0.3}$	$6.82^{+0.02}_{-0.02}$	$1.7^{+0.1}_{-0.1}$	$23.0^{+1.3}_{-1.2}$	$6.72^{+0.05}_{-0.05}$	
184	17.00	$26.8^{+1.0}_{-0.9}$	$5.94^{+0.06}_{-0.06}$	$2.5^{+0.5}_{-0.5}$	$22.7^{+3.7}_{-2.9}$	$6.05^{+0.11}_{-0.12}$	
185	17.00	$19.1^{+0.8}_{-0.8}$	$6.53^{+0.07}_{-0.06}$	$2.2^{+0.5}_{-0.5}$	$18.2^{+1.0}_{-2.3}$	$6.58^{+0.15}_{-0.14}$	
188	17.00	$19.3^{+0.5}_{-0.5}$	$7.00^{+0.03}_{-0.03}$	$1.6^{+0.2}_{-0.2}$	$21.9^{+1.6}_{-1.4}$	$6.88^{+0.07}_{-0.07}$	
189	17.00	$20.8^{+0.6}_{-0.6}$	$6.50^{+0.04}_{-0.04}$	$1.8^{+0.2}_{-0.2}$	$22.6^{+2.0}_{-1.8}$	$6.43^{+0.08}_{-0.08}$	
190	17.00	$21.2^{+0.3}_{-0.3}$	$8.02^{+0.02}_{-0.02}$	$2.2^{+0.1}_{-0.1}$	$20.1^{+0.9}_{-0.8}$	$8.08^{+0.04}_{-0.04}$	
191	17.00	$21.4^{+1.4}_{-1.5}$	$5.88^{+0.10}_{-0.10}$	$1.3^{+0.7}_{-0.6}$	$26.4^{+8.2}_{-5.3}$	$5.71^{+0.19}_{-0.21}$	
192	17.00	$20.8^{+0.7}_{-0.6}$	$5.80^{+0.06}_{-0.06}$	$2.4^{+0.5}_{-0.5}$	$18.8^{+2.1}_{-2.1}$	$5.88^{+0.11}_{-0.11}$	
193	17.00	$20.3^{+0.5}_{-0.5}$	$6.71^{+0.04}_{-0.04}$	$1.4^{+0.2}_{-0.2}$	$24.4^{+2.3}_{-2.0}$	$6.54^{+0.08}_{-0.08}$	
194	17.00	-	-	$1.4^{+0.1}_{-0.1}$	$21.3^{+0.9}_{-0.8}$	$7.88^{+0.04}_{-0.04}$	
196	17.00	$21.5^{+0.6}_{-0.6}$	$7.00^{+0.04}_{-0.04}$	$1.4^{+0.3}_{-0.2}$	$26.0^{+2.8}_{-2.3}$	$6.84^{+0.08}_{-0.08}$	
197	17.00	$20.7^{+0.4}_{-0.4}$	$6.84^{+0.03}_{-0.03}$	$1.7^{+0.2}_{-0.2}$	$22.6^{+1.3}_{-1.2}$	$6.76^{+0.05}_{-0.05}$	
198	16.77	$16.1^{+0.7}_{-0.7}$	$6.91^{+0.07}_{-0.07}$	$1.6^{+0.4}_{-0.3}$	$18.4^{+2.9}_{-2.7}$	$6.75^{+0.19}_{-0.16}$	
199	17.00	$20.8^{+1.6}_{-1.5}$	$6.25^{+0.11}_{-0.12}$	$1.7^{+0.7}_{-0.6}$	$22.8^{+7.6}_{-5.1}$	$6.16^{+0.27}_{-0.26}$	
200	17.00	-	-	$2.2^{+0.1}_{-0.1}$	$22.3^{+0.7}_{-0.6}$	$7.07^{+0.03}_{-0.03}$	
201	17.00	$22.1^{+0.2}_{-0.2}$	$7.88^{+0.01}_{-0.01}$	$2.0^{+0.1}_{-0.1}$	$22.5^{+0.6}_{-0.6}$	$7.86^{+0.02}_{-0.02}$	
203	17.00	-	-	$1.5^{+0.1}_{-0.1}$	$28.0^{+1.3}_{-1.2}$	$6.87^{+0.04}_{-0.04}$	
204	17.00	$19.7^{+0.3}_{-0.3}$	$7.91^{+0.03}_{-0.03}$	$2.1^{+0.2}_{-0.2}$	$19.2^{+1.1}_{-1.0}$	$7.93^{+0.06}_{-0.06}$	
205	17.00	-	-	$1.5^{+0.1}_{-0.1}$	$27.3^{+1.3}_{-1.2}$	$7.50^{+0.04}_{-0.04}$	
206	17.00	$22.4^{+0.9}_{-0.9}$	$6.39^{+0.06}_{-0.05}$	$1.8^{+0.3}_{-0.3}$	$23.7^{+3.2}_{-2.6}$	$6.35^{+0.11}_{-0.11}$	
207	17.00	$21.0^{+0.3}_{-0.3}$	$6.88^{+0.02}_{-0.02}$	$2.0^{+0.2}_{-0.2}$	$20.8^{+1.1}_{-1.0}$	$6.89^{+0.05}_{-0.05}$	
208	17.00	$19.2^{+0.9}_{-0.9}$	$7.59^{+0.07}_{-0.06}$	$2.0^{+0.5}_{-0.4}$	$19.0^{+3.4}_{-2.8}$	$7.61^{+0.19}_{-0.18}$	
212	20.14	-	-	$1.1^{+0.3}_{-0.3}$	$28.7^{+4.1}_{-3.3}$	$6.37^{+0.10}_{-0.10}$	
213	17.61	-	-	$1.6^{+0.1}_{-0.1}$	$20.9^{+0.8}_{-0.8}$	$8.17^{+0.04}_{-0.04}$	
217	17.00	$21.5^{+0.4}_{-0.4}$	$7.59^{+0.03}_{-0.03}$	$2.3^{+0.2}_{-0.2}$	$19.9^{+1.2}_{-1.1}$	$7.66^{+0.06}_{-0.06}$	
220	17.00	$20.7^{+0.6}_{-0.6}$	$7.64^{+0.05}_{-0.05}$	$2.3^{+0.4}_{-0.3}$	$19.0^{+2.0}_{-1.7}$	$7.72^{+0.10}_{-0.10}$	
221	17.00	$20.8^{+0.3}_{-0.3}$	$6.89^{+0.02}_{-0.02}$	$2.1^{+0.1}_{-0.1}$	$20.2^{+0.8}_{-0.8}$	$6.92^{+0.04}_{-0.04}$	

Continued on the next page...

Table 3 – Continued.

HRS	D Mpc	$\beta=2$			$\beta=\text{free}$	
		T K	$\log(M_{\text{dust}})$ M_{\odot}	β	T K	$\log(M_{\text{dust}})$ M_{\odot}
222	17.00	21.0 ^{+1.3} _{-1.3}	6.01 ^{+0.10} _{-0.09}	2.5 ^{+0.8} _{-0.7}	18.3 ^{+4.2} _{-3.2}	6.14 ^{+0.21} _{-0.20}
223	17.00	16.8 ^{+1.2} _{-1.2}	6.32 ^{+0.12} _{-0.11}	1.2 ^{+0.7} _{-0.6}	21.2 ^{+6.3} _{-4.4}	6.07 ^{+0.26} _{-0.25}
224	17.00	19.2 ^{+0.9} _{-0.9}	6.72 ^{+0.07} _{-0.07}	2.0 ^{+0.5} _{-0.5}	19.5 ^{+2.8} _{-2.8}	6.71 ^{+0.17} _{-0.16}
226	17.00	20.5 ^{+0.5} _{-0.6}	6.45 ^{+0.04} _{-0.04}	1.7 ^{+0.2} _{-0.2}	22.2 ^{+1.9} _{-1.7}	6.38 ^{+0.08} _{-0.08}
227	15.27	-	-	0.7 ^{+0.2} _{-0.2}	29.9 ^{+3.8} _{-3.1}	6.62 ^{+0.09} _{-0.10}
230	17.00	21.2 ^{+0.5} _{-0.5}	6.64 ^{+0.04} _{-0.04}	1.7 ^{+0.2} _{-0.2}	23.1 ^{+1.9} _{-1.7}	6.56 ^{+0.07} _{-0.07}
231	17.00	26.1 ^{+0.8} _{-0.8}	5.61 ^{+0.04} _{-0.04}	2.2 ^{+0.4} _{-0.4}	24.8 ^{+3.5} _{-2.9}	5.65 ^{+0.09} _{-0.09}
232	17.00	22.4 ^{+0.6} _{-0.6}	6.38 ^{+0.04} _{-0.04}	2.2 ^{+0.4} _{-0.3}	20.9 ^{+2.9} _{-2.0}	6.44 ^{+0.09} _{-0.10}
233	17.00	22.0 ^{+0.5} _{-0.5}	6.94 ^{+0.03} _{-0.03}	2.2 ^{+0.2} _{-0.2}	20.8 ^{+1.5} _{-1.3}	6.99 ^{+0.07} _{-0.07}
237	17.00	21.9 ^{+0.6} _{-0.6}	6.77 ^{+0.04} _{-0.04}	2.0 ^{+0.3} _{-0.3}	21.6 ^{+2.0} _{-1.8}	6.78 ^{+0.08} _{-0.08}
238	15.94	21.4 ^{+1.7} _{-1.8}	5.81 ^{+0.12} _{-0.12}	0.7 ^{+0.7} _{-0.7}	36.1 ^{+26.7} _{-10.3}	5.40 ^{+0.27} _{-0.37}
239	17.00	22.7 ^{+0.3} _{-0.3}	7.01 ^{+0.02} _{-0.02}	2.1 ^{+0.1} _{-0.1}	22.2 ^{+0.8} _{-0.8}	7.03 ^{+0.04} _{-0.04}
242	17.00	21.2 ^{+0.6} _{-0.6}	6.90 ^{+0.04} _{-0.04}	1.4 ^{+0.3} _{-0.3}	25.6 ^{+3.0} _{-2.5}	6.74 ^{+0.09} _{-0.09}
243	17.00	16.4 ^{+1.0} _{-0.9}	7.13 ^{+0.09} _{-0.08}	2.7 ^{+0.8} _{-0.6}	13.5 ^{+2.9} _{-2.6}	7.38 ^{+0.34} _{-0.26}
244	17.00	-	-	2.2 ^{+0.1} _{-0.1}	20.6 ^{+0.7} _{-0.7}	7.34 ^{+0.04} _{-0.04}
246	17.00	21.0 ^{+0.4} _{-0.4}	7.39 ^{+0.03} _{-0.03}	1.8 ^{+0.2} _{-0.2}	22.6 ^{+1.4} _{-1.3}	7.32 ^{+0.06} _{-0.06}
247	17.00	-	-	1.8 ^{+0.1} _{-0.1}	22.6 ^{+0.8} _{-0.8}	7.66 ^{+0.03} _{-0.03}
252	23.13	18.0 ^{+1.4} _{-1.4}	6.87 ^{+0.11} _{-0.10}	1.0 ^{+0.4} _{-0.3}	27.6 ^{+5.9} _{-4.5}	6.47 ^{+0.16} _{-0.16}
254	17.00	20.3 ^{+1.0} _{-1.0}	7.37 ^{+0.07} _{-0.07}	2.1 ^{+0.4} _{-0.4}	19.6 ^{+3.0} _{-2.5}	7.41 ^{+0.15} _{-0.14}
255	17.00	17.1 ^{+1.3} _{-1.2}	6.99 ^{+0.11} _{-0.11}	0.6 ^{+0.6} _{-0.5}	32.7 ^{+18.6} _{-9.2}	6.36 ^{+0.30} _{-0.33}
257	17.00	16.9 ^{+0.8} _{-0.8}	7.25 ^{+0.08} _{-0.08}	1.8 ^{+0.5} _{-0.5}	18.2 ^{+3.2} _{-2.7}	7.17 ^{+0.20} _{-0.18}
258	17.73	31.2 ^{+1.1} _{-1.1}	5.35 ^{+0.04} _{-0.04}	2.1 ^{+0.3} _{-0.3}	29.6 ^{+4.3} _{-3.4}	5.38 ^{+0.08} _{-0.09}
259	17.00	-	-	1.0 ^{+0.3} _{-0.3}	29.7 ^{+6.0} _{-4.5}	6.66 ^{+0.14} _{-0.14}
260	17.00	23.0 ^{+0.3} _{-0.3}	7.03 ^{+0.02} _{-0.02}	2.0 ^{+0.1} _{-0.1}	23.3 ^{+1.0} _{-0.9}	7.02 ^{+0.04} _{-0.04}
261	16.54	17.3 ^{+0.7} _{-0.7}	6.83 ^{+0.07} _{-0.06}	1.9 ^{+0.4} _{-0.4}	18.0 ^{+2.3} _{-2.0}	6.79 ^{+0.14} _{-0.13}
262	17.00	21.8 ^{+0.6} _{-0.6}	7.07 ^{+0.04} _{-0.04}	1.6 ^{+0.2} _{-0.2}	24.8 ^{+2.2} _{-1.9}	6.97 ^{+0.07} _{-0.07}
263	17.27	18.2 ^{+0.7} _{-0.7}	8.02 ^{+0.07} _{-0.07}	1.7 ^{+0.4} _{-0.4}	19.9 ^{+2.7} _{-2.3}	7.94 ^{+0.13} _{-0.13}
264	18.17	16.7 ^{+0.6} _{-0.6}	6.55 ^{+0.06} _{-0.06}	1.6 ^{+0.4} _{-0.3}	19.1 ^{+2.1} _{-2.1}	6.41 ^{+0.13} _{-0.13}
265	21.49	23.2 ^{+0.7} _{-0.7}	6.38 ^{+0.04} _{-0.04}	1.9 ^{+0.3} _{-0.3}	23.7 ^{+2.5} _{-2.1}	6.36 ^{+0.08} _{-0.08}
266	21.30	17.5 ^{+1.2} _{-1.2}	7.66 ^{+0.09} _{-0.09}	1.1 ^{+0.4} _{-0.4}	25.0 ^{+5.4} _{-4.1}	7.29 ^{+0.18} _{-0.18}
267	16.84	18.7 ^{+0.9} _{-0.9}	6.99 ^{+0.06} _{-0.06}	1.5 ^{+0.3} _{-0.3}	23.1 ^{+3.2} _{-2.8}	6.77 ^{+0.13} _{-0.12}
268	17.00	-	-	1.8 ^{+0.1} _{-0.1}	24.6 ^{+0.9} _{-0.8}	6.93 ^{+0.03} _{-0.03}
270	17.70	21.2 ^{+0.9} _{-0.9}	7.11 ^{+0.06} _{-0.06}	2.1 ^{+0.4} _{-0.4}	20.4 ^{+2.9} _{-2.4}	7.14 ^{+0.14} _{-0.14}
271	17.00	-	-	1.3 ^{+0.2} _{-0.2}	24.3 ^{+2.6} _{-2.2}	6.66 ^{+0.09} _{-0.09}
273	17.00	18.9 ^{+0.6} _{-0.6}	7.11 ^{+0.05} _{-0.05}	1.8 ^{+0.3} _{-0.3}	20.0 ^{+2.0} _{-1.8}	7.05 ^{+0.10} _{-0.09}
274	17.00	17.3 ^{+0.4} _{-0.4}	6.90 ^{+0.04} _{-0.04}	2.1 ^{+0.3} _{-0.3}	17.0 ^{+1.3} _{-1.2}	6.92 ^{+0.09} _{-0.09}
275	22.37	-	-	1.5 ^{+0.2} _{-0.2}	27.1 ^{+2.0} _{-1.7}	7.02 ^{+0.06} _{-0.06}
276	17.00	21.5 ^{+0.6} _{-0.6}	6.69 ^{+0.04} _{-0.04}	1.6 ^{+0.2} _{-0.2}	24.7 ^{+2.3} _{-2.0}	6.57 ^{+0.08} _{-0.08}
277	17.00	22.0 ^{+1.4} _{-1.3}	5.64 ^{+0.11} _{-0.11}	2.9 ^{+1.4} _{-1.1}	17.6 ^{+5.6} _{-3.9}	5.83 ^{+0.25} _{-0.25}
279	17.00	16.8 ^{+0.8} _{-0.8}	7.08 ^{+0.07} _{-0.07}	1.2 ^{+0.4} _{-0.3}	22.1 ^{+3.5} _{-2.9}	6.79 ^{+0.15} _{-0.14}
280	17.00	22.3 ^{+0.4} _{-0.4}	6.51 ^{+0.02} _{-0.02}	1.9 ^{+0.2} _{-0.2}	23.2 ^{+1.3} _{-1.2}	6.48 ^{+0.05} _{-0.05}
281	17.00	20.0 ^{+0.8} _{-0.8}	5.95 ^{+0.06} _{-0.06}	2.2 ^{+0.5} _{-0.4}	19.0 ^{+2.7} _{-2.3}	6.00 ^{+0.14} _{-0.13}
285	17.00	22.5 ^{+0.3} _{-0.3}	7.31 ^{+0.02} _{-0.02}	2.0 ^{+0.1} _{-0.1}	22.4 ^{+0.9} _{-0.9}	7.32 ^{+0.04} _{-0.04}
286	17.00	16.7 ^{+1.3} _{-1.2}	6.75 ^{+0.15} _{-0.16}	0.8 ^{+0.8} _{-0.7}	23.9 ^{+9.2} _{-5.6}	6.41 ^{+0.27} _{-0.28}
287	17.00	21.2 ^{+0.5} _{-0.5}	6.95 ^{+0.03} _{-0.03}	1.7 ^{+0.2} _{-0.2}	23.3 ^{+1.6} _{-1.5}	6.86 ^{+0.06} _{-0.06}
288	15.91	19.2 ^{+0.5} _{-0.5}	7.11 ^{+0.04} _{-0.04}	2.0 ^{+0.2} _{-0.2}	19.1 ^{+1.6} _{-1.4}	7.11 ^{+0.09} _{-0.09}
289	23.97	21.7 ^{+0.4} _{-0.4}	7.45 ^{+0.02} _{-0.02}	1.8 ^{+0.1} _{-0.1}	22.8 ^{+1.1} _{-1.0}	7.41 ^{+0.04} _{-0.04}
290	16.23	25.1 ^{+0.5} _{-0.5}	6.25 ^{+0.03} _{-0.03}	2.1 ^{+0.3} _{-0.2}	24.5 ^{+1.8} _{-1.8}	6.27 ^{+0.06} _{-0.06}
292	17.50	24.4 ^{+0.4} _{-0.4}	6.87 ^{+0.02} _{-0.02}	2.1 ^{+0.1} _{-0.1}	23.8 ^{+1.1} _{-1.1}	6.89 ^{+0.04} _{-0.04}
293	15.60	-	-	1.6 ^{+0.1} _{-0.1}	24.3 ^{+1.4} _{-1.3}	6.73 ^{+0.05} _{-0.05}
294	22.97	20.1 ^{+0.5} _{-0.5}	6.94 ^{+0.03} _{-0.03}	1.5 ^{+0.2} _{-0.2}	23.7 ^{+1.7} _{-1.5}	6.80 ^{+0.06} _{-0.06}
295	16.46	21.8 ^{+0.5} _{-0.5}	7.80 ^{+0.03} _{-0.03}	2.0 ^{+0.2} _{-0.2}	21.9 ^{+1.3} _{-1.2}	7.80 ^{+0.06} _{-0.06}
296	15.20	22.6 ^{+1.8} _{-1.7}	5.76 ^{+0.11} _{-0.11}	0.9 ^{+0.5} _{-0.5}	38.0 ^{+20.3} _{-10.0}	5.38 ^{+0.23} _{-0.28}
297	21.54	-	-	1.6 ^{+0.1} _{-0.1}	22.4 ^{+1.3} _{-1.2}	7.36 ^{+0.05} _{-0.05}
298	20.27	24.4 ^{+0.4} _{-0.4}	6.68 ^{+0.02} _{-0.02}	2.1 ^{+0.2} _{-0.1}	23.3 ^{+1.3} _{-1.2}	6.72 ^{+0.05} _{-0.05}
299	16.73	18.4 ^{+0.9} _{-0.9}	7.16 ^{+0.07} _{-0.07}	1.4 ^{+0.4} _{-0.3}	22.7 ^{+3.3} _{-2.7}	6.97 ^{+0.12} _{-0.12}
300	19.34	19.5 ^{+0.8} _{-0.8}	6.26 ^{+0.07} _{-0.07}	1.6 ^{+0.5} _{-0.5}	21.6 ^{+4.0} _{-3.0}	6.17 ^{+0.15} _{-0.15}

Continued on the next page...

Table 3 – Continued.

HRS	D Mpc	$\beta=2$			$\beta=\text{free}$	
		T K	$\log(M_{dust})$ M_{\odot}	β	T K	$\log(M_{dust})$ M_{\odot}
301	19.71	17.4 ^{+0.9} _{-1.0}	7.43 ^{+0.08} _{-0.07}	1.1 ^{+0.4} _{-0.3}	24.1 ^{+4.1} _{-3.2}	7.10 ^{+0.15} _{-0.15}
302	20.61	15.6 ^{+1.1} _{-1.0}	7.07 ^{+0.09} _{-0.09}	1.0 ^{+0.4} _{-0.3}	25.0 ^{+5.5} _{-4.4}	6.57 ^{+0.19} _{-0.17}
303	24.53	26.8 ^{+0.6} _{-0.6}	6.49 ^{+0.03} _{-0.03}	2.1 ^{+0.3} _{-0.2}	26.3 ^{+2.5} _{-2.1}	6.51 ^{+0.07} _{-0.07}
304	19.57	19.1 ^{+0.4} _{-0.4}	7.10 ^{+0.03} _{-0.03}	2.0 ^{+0.2} _{-0.2}	19.2 ^{+1.2} _{-1.2}	7.09 ^{+0.07} _{-0.07}
305	16.73	18.2 ^{+1.3} _{-1.3}	5.98 ^{+0.13} _{-0.13}	2.2 ^{+1.0} _{-0.8}	17.5 ^{+5.0} _{-3.7}	6.03 ^{+0.29} _{-0.27}
306	16.23	23.2 ^{+1.5} _{-1.5}	6.61 ^{+0.08} _{-0.08}	2.6 ^{+0.7} _{-0.6}	19.4 ^{+4.0} _{-3.1}	6.77 ^{+0.19} _{-0.18}
307	17.74	19.1 ^{+0.7} _{-0.7}	7.71 ^{+0.05} _{-0.05}	1.6 ^{+0.3} _{-0.3}	21.5 ^{+2.2} _{-2.0}	7.60 ^{+0.10} _{-0.09}
309	19.76	-	-	1.0 ^{+0.2} _{-0.2}	28.4 ^{+3.4} _{-2.8}	6.11 ^{+0.09} _{-0.09}
310	24.54	21.3 ^{+0.5} _{-0.5}	7.07 ^{+0.04} _{-0.04}	2.3 ^{+0.3} _{-0.3}	19.9 ^{+1.6} _{-1.5}	7.13 ^{+0.07} _{-0.07}
311	21.31	19.1 ^{+0.7} _{-0.7}	7.50 ^{+0.05} _{-0.05}	2.0 ^{+0.3} _{-0.3}	19.4 ^{+2.2} _{-2.0}	7.49 ^{+0.12} _{-0.11}
313	21.29	16.9 ^{+0.8} _{-0.8}	7.27 ^{+0.06} _{-0.06}	1.5 ^{+0.3} _{-0.3}	20.5 ^{+2.9} _{-2.7}	7.06 ^{+0.15} _{-0.13}
314	19.84	-	-	1.0 ^{+0.2} _{-0.2}	27.6 ^{+3.4} _{-2.8}	6.57 ^{+0.09} _{-0.09}
315	20.57	20.7 ^{+2.7} _{-2.8}	6.24 ^{+0.21} _{-0.19}	-	-	-
317	24.51	17.4 ^{+1.0} _{-0.9}	6.42 ^{+0.10} _{-0.10}	1.8 ^{+0.8} _{-0.7}	18.7 ^{+4.8} _{-3.6}	6.34 ^{+0.26} _{-0.23}
318	19.57	-	-	1.4 ^{+0.2} _{-0.2}	25.1 ^{+1.9} _{-1.7}	6.80 ^{+0.06} _{-0.06}
319	19.54	-	-	1.1 ^{+0.3} _{-0.3}	26.3 ^{+3.4} _{-2.8}	6.98 ^{+0.10} _{-0.11}
320	22.61	-	-	1.1 ^{+0.3} _{-0.3}	25.2 ^{+4.0} _{-3.4}	7.27 ^{+0.14} _{-0.13}
321	22.59	23.5 ^{+0.4} _{-0.4}	6.55 ^{+0.02} _{-0.02}	1.9 ^{+0.2} _{-0.2}	24.6 ^{+1.4} _{-1.3}	6.51 ^{+0.05} _{-0.05}
322	21.50	14.4 ^{+1.4} _{-1.3}	7.51 ^{+0.15} _{-0.15}	1.7 ^{+1.5} _{-0.9}	16.0 ^{+6.6} _{-5.8}	7.38 ^{+0.70} _{-0.39}
323	23.43	-	-	1.7 ^{+0.1} _{-0.1}	22.8 ^{+0.9} _{-0.9}	7.11 ^{+0.04} _{-0.04}